2019

Robust Impedance Control of a Four Degree of Freedom Exercise Robot

Santino Joseph Bianco

Recommended Citation

Bianco, Santino Joseph, "Robust Impedance Control of a Four Degree of Freedom Exercise Robot" (2019). *ETD Archive*. 1141.
https://engagedscholarship.csuohio.edu/etdarchive/1141

ROBUST IMPEDANCE CONTROL OF

A FOUR DEGREE OF FREEDOM

EXERCISE ROBOT

SANTINO BIANCO

Bachelor of Science in Mechanical Engineering

Cleveland State University

May 2018

submitted in partial fulfillment of requirements for the degree

MASTERS OF SCIENCE IN MECHANICAL ENGINEERING

at the

CLEVELAND STATE UNIVERSITY

MAY 2019

We hereby approve this thesis for

SANTINO BIANCO

Candidate for the Master of Science in Mechanical Engineering degree for the

Department of Mechanical Engineering

and the CLEVELAND STATE UNIVERSITY

College of Graduate Studies

Thesis Chairperson, Dr. Hanz Richter

Department & Date

Thesis Committee Member, Dr. Dan Simon

Department & Date

Thesis Committee Member, Dr. Jerzy T. Sawicki

Department & Date

Student's Date of Defense: May 7, 2019

ACKNOWLEDGMENTS

ROBUST IMPEDANCE CONTROL OF A FOUR DEGREE OF FREEDOM
EXERCISE ROBOT

SANTINO BIANCO

ABSTRACT

The CSU 4OptimX exercise robot provides a platform for future research into advanced exercise and rehabilitation. The robot and its control system will autonomously modify reference trajectories and impedances on the basis of an optimization criterion and physiological feedback. To achieve this goal, a robust impedance control system with trajectory tracking must be implemented as the foundational control scheme. Two control laws will be compared, sliding mode and $\mathcal{H}_\infty$ control.

The above robust control laws are combined with underlying impedance control laws to overcome uncertain plant model parameters and disturbance anomalies affecting the input signal. The sliding mode control law is synthesized based on a nominal plant model due to its inherent nature of overcoming unspecified, un-modeled dynamics and disturbances. Implementation of the $\mathcal{H}_\infty$ control law uses weights as well as the nominal plant, a structured parametric uncertainty model of the plant, and a model with multiplicative uncertainty. The performance and practicality of each controller is discussed as well as the challenges associated with attempts to implement controllers successfully onto the robot.

The findings of this thesis indicate that the closed loop controller with sliding mode is the superior control scheme due to its abilities to counter non-linearities. It is chosen as the platform control scheme. The 2 out of 3 $\mathcal{H}_\infty$ controllers performed well in simulation but only one was able to successfully control the robot. Challenges associated with $\mathcal{H}_\infty$ control implementation toward impedance control include defining proper weight shapes that balance performance and practicality. This challenge is a starting point for future research into general weight shape determination for $\mathcal{H}_\infty$

robust impedance control.

TABLE OF CONTENTS

LIST OF TABLES

LIST OF FIGURES

CHAPTER I

Introduction

Impedance control is an approach to the control of the dynamic interaction between a manipulator and its environment. It is different from force and position control techniques that act on the feedback error between an actual and desired value. Impedance control aims to regulate the ratio of force output to motion input of a desired impedance behavior [5]. This characteristic makes it a suitable control approach for environment manipulation and human-machine interaction in robotics. Given a motion input, an impedance force is imparted at the interaction point between the machine and an object/human. All achievable impedance forces can be characterized by an impedance equation where M is the mass, B is the damping, K is the spring constant, and x is the position along with its subsequent time derivatives.

$$f(x, \dot{x}, \ddot{x}) = M\ddot{x} + B\dot{x} + Kx \qquad (1.1)$$

Simple impedance regulation involves integrating the function above with a plant in order to imitate a prescribed behavior. Essentially, impedance control is equivalent to adding a physical mass-spring-damper to a plant. However, it is evident that the mass-spring-damper effect is entirely virtual and produces the behavior through a control input.

(a) Plant (b) Desired Behavior of Plant
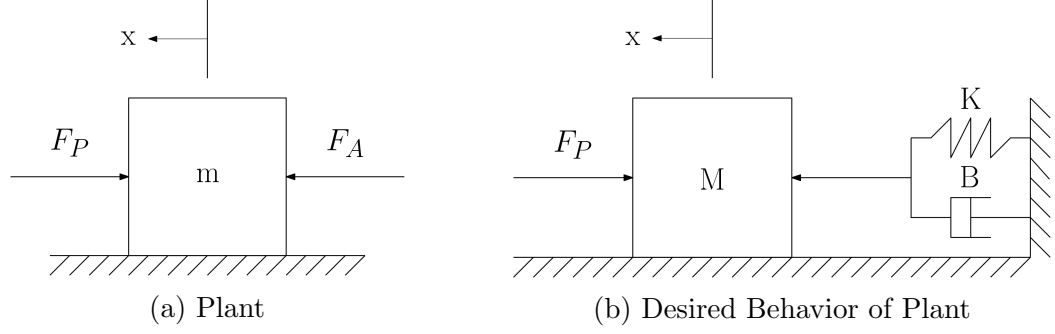
Figure 1: Impedance Control Interpretation

In order to explain impedance control implementation, an elementary example shows how a simple impedance controller is constructed for a mass with two input forces. Beginning with a dynamic equation of a mass, an actuator force, F_A, is added in one direction and a force applied by a person, F_P, is added in the opposite direction, as seen in Figure 1a.

$$m\ddot{x} = F_A - F_P \tag{1.2}$$

For the plant to produce the desired impedance shown mathematically in (1.1) and physically in Figure 1b, the impedance function must be set equal to the force of the person pushing on the mass. This mathematical relation means that the force produced by the person pushing on the mass must equal a general impedance behavior. It is important to set the impedance function equal to a measured or observed force for increased performance in obtaining the desired impedance.

$$M\ddot{x} + B\dot{x} + Kx = -F_P \tag{1.3}$$

In order to combine the impedance function with the plant, both accelerations must be set equal to one another. This merging of functions allows for a virtual mass-spring-damper to be added to the plant.

$$\frac{F_A - F_P}{m} = \frac{-F_P - Kx - B\dot{x}}{M} \tag{1.4}$$

2

Solving for the inverse dynamics where F_A is now the controller output force yields a simple impedance controller.

$$F_A = \left(1 - \frac{m}{M}\right) F_P - \frac{mK}{M} x - \frac{mB}{M} \dot{x} \qquad (1.5)$$

This controller and plant yields a closed loop control system shown below.
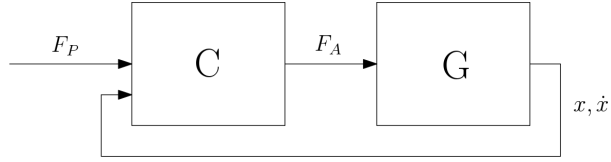
Figure 2: Simple Impedance Closed Loop Block Diagram

Simple impedance controllers are practical where exact impedance is not required. For increased accuracy in achieving a desired impedance, additional control laws, such as the laws used in this thesis, are necessary to achieve desired behavior during manipulator interaction. These strategies are needed due to modeling errors and disturbances that affect the plant from producing the exact impedance that equation (1.5) theoretically dictates. Non-robust, model-based controllers, such as this simple impedance controller, generally fall victim to such problems. Those control strategies are implemented on a custom exercise machine at Cleveland State University, the CSU 4OptimX.

1.1 Motivation

Exercise machines produce forces that apply stress to selected muscle groups. These force vectors are normally static, such as weights, or linearly dynamic, such as resistance bands. Common exercise machines have the ability to change the amount of resistance but not in real time. Using impedance control with electric motors to dynamically modulate the force vector presented to the user in real time has many

benefits to different applications and in different industries. Examples of applications will be presented in the upcoming section.

The impedance control application presented in this thesis is a stepping stone in a much larger research effort. Currently, much of the impedance control applications are in rehabilitation robotics. There are few to no examples where impedance control is applied to exercise machines for able-bodied individuals. This presents a path for growth in the technology of exercise machines. In an effort to create advanced exercise machines, this application of robust impedance control will provide the footing for a larger research effort into developing adaptive exercise machines. Adaptive exercise machines will be capable of adjusting impedance parameters and trajectories based on biological input from the user.

The goal of this thesis is to implement a robust impedance control system with trajectory tracking as the foundational control scheme. A secondary goal is to compare the performance and practicality of two robust control laws toward impedance control: sliding mode and $\mathcal{H}_\infty$ control. The need for comparison arises from the lack in knowledge of using $\mathcal{H}_\infty$ control toward achieving accurate impedance control. This thesis will answer the question of whether an optimized, robust, fixed gain controller can outperform a robust non-linear controller for the given application.

1.2   Literature Review

Applications involving impedance control can be a broad topic to describe concisely. Therefore, previous research is broken down according to applications involving similar machines to the one described in this thesis, applications of those machines to different industries, and applications that show where this research will be headed in the future. Examples of these applications include upper body rehabilitation robots, exercise machines in space, and robots utilizing muscle activation

feedback.

1.2.1 Upper Body Rehabilitation Robots

Impedance control for rehabilitation robots has been achieved in various applications throughout recent history. The control theory can be used in robotics to aid movement and apply varying degrees of force, simultaneously, for user rehabilitation. In this cited case, a 3 degree of freedom robotic arm utilizing impedance control theory aids the user in varying degrees during upper body exercises [13].
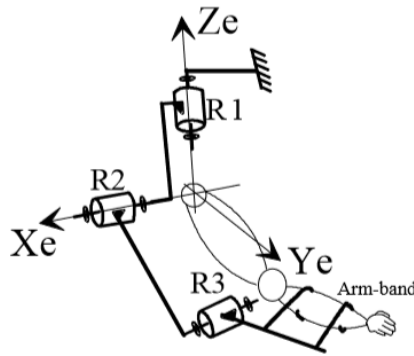
Figure 3: Rehabilitation Robot with Hybrid Force/Impedance Control [13]

The resulting goal of the "Active-Assist" mode, which utilizes impedance control, is to keep the user on a predefined trajectory as the user moves the robotic arm through a predefined space. Similar research by Ju et al. uses a hybrid force/position controller to maintain wrist position to a required trajectory while simultaneously providing a resistive force tangential to the path [6].

(a) Robot   (b) Schematic
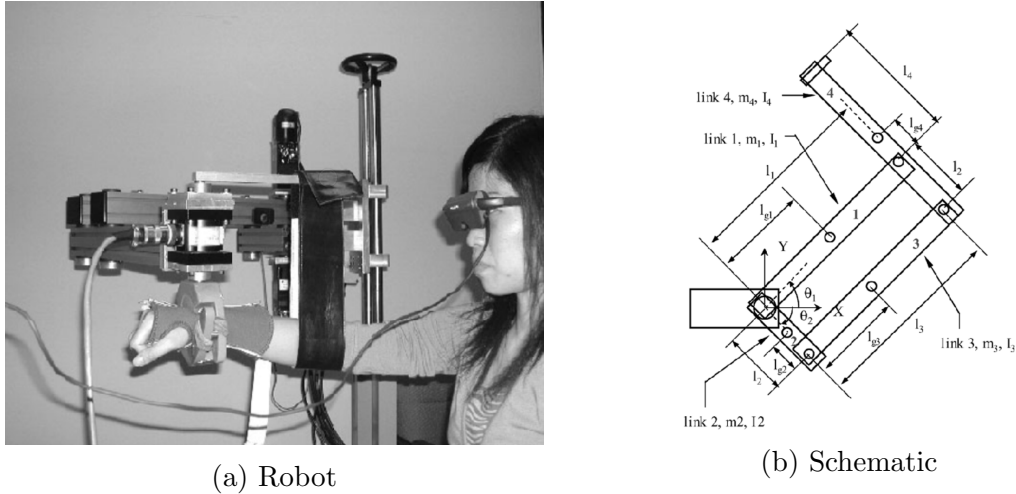
Figure 4: Rehabilitation Robot with Hybrid Force/Position Control [6]

Although this example does not include impedance control, the design of this robot and other impedance control robots is of great value when describing where impedance control and rehabilitation efforts lie in the past and present. Many of the rehabilitation robots, such as the ones listed previously, are more comparable to exoskeletons in the sense that they operate next to the arm and its joints either to aid or to resist movement. The robot presented in this thesis will aid the user by resisting movement from an individual standing opposite to the robotic arm. Many able-bodied exercise machines, as opposed to rehabilitation machines, have this approach.

It is also notable to add that there is not an abundance of research pertaining to the development of gym-style exercise machines utilizing electric motors with impedance control such as the CSU 4OptimX. One such recent example includes work done by Richter et al. at Cleveland State University toward impedance control and energy regeneration on an electric motor controlled rowing machine [20], [16], [2].
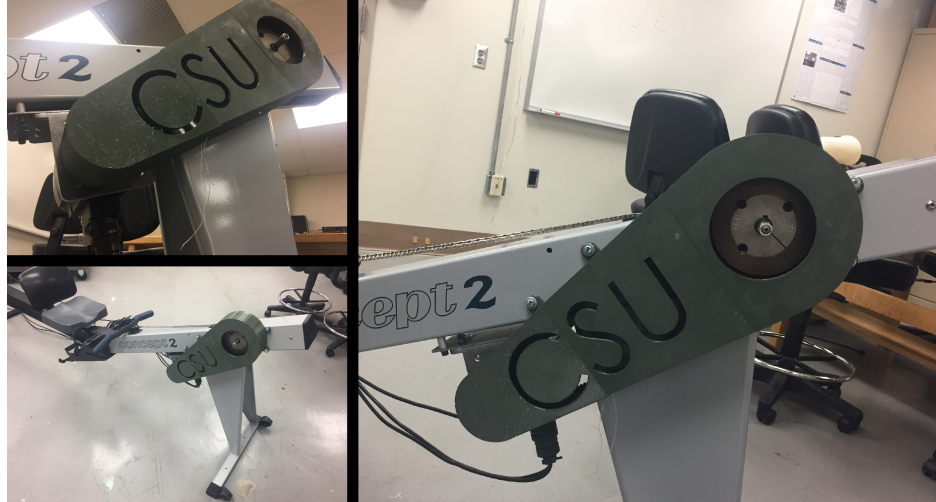
Figure 5: Electric Motor-controlled Rowing Machine [2]

Another decades-old application includes an electric motor-aided weight stack that provides asymmetric force output to the user [17]. The device is an attachment to a weight stack and uses force control to apply added force when lowering the weight stack. This addition of force is useful for eccentric muscle movements during exercise to increase muscle activation during the full range of motion.

(a) Full View
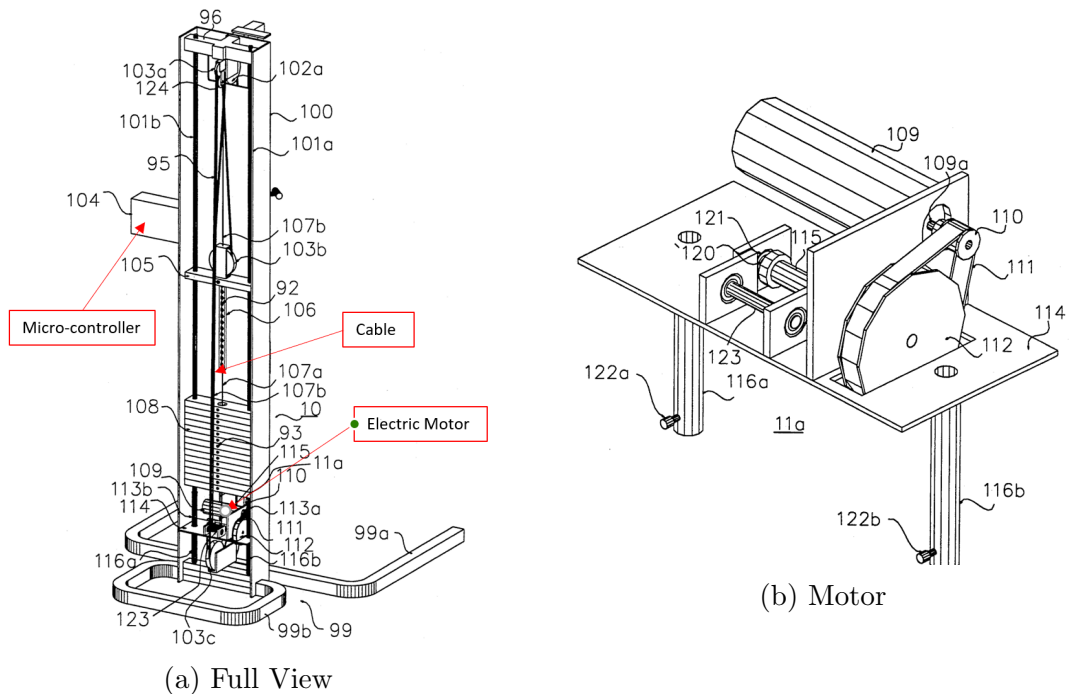
(b) Motor

Figure 6: Electric Motor-aided Weight Stack [17]

The rowing machine is most similar to the CSU 4OptimX in the sense that electric motors will replace weights, not aid them. Also, using only electric motors gives full control of the weight to the control system. This provides an extra measure of safety for the user, no matter the application.

1.2.2 Exercise Machines in Space

Exercising in space is slightly more complicated than on Earth. Since the International Space Station (ISS) is falling around Earth, so is everything else in it. This concept creates the illusion of weightlessness. Moreover, any masses used in traditional, Earth-based exercise cannot be used because they would appear to be weightless as well. Only the inertia effects of the mass would provide resistance to the user. Therefore, any resistances used for weight training or to aid in other exercises, such as staying positioned on a treadmill, must be produced by other sources than gravity. Once such paper describes many of the exercise devices used on the space station and their effectiveness [15].

One such exercise machine is the Advanced Resistive Exercise Device (ARED). This device operates on two different force producing mechanisms. Once mechanism is a lever arm attached to a vacuum piston assembly. The other is the use of a flywheel and its inertial properties to mimic the inertial load of a free weight. This device is meant for lower body exercises such as squats, dead lifts, and calve raises, but can be used for all muscle groups. It can produce up to 600 lbs. of force to the user [18]. This device is retired from the ISS. It was replaced by the device presented next.
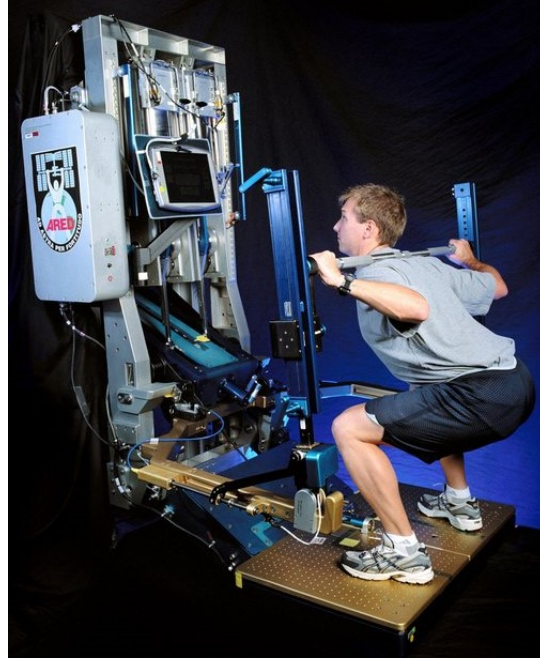
Figure 7: Advanced Resistive Exercise Device (ARED)

Another exercise device used on the space station is the Interim Resistive Exercise Device (iRED) [1]. The iRED contains a series of 16 flex packs stacked vertically inside cylindrical canisters and is designed to provide resistance training for crew members in micro-gravity. A flex pack consists of a ring disk aluminum outer rim, with rubber spokes protruding inward toward a center hub. The flex packs revolve about a metal axle. When the metal axle is turned, the rubber spokes are stretched, increasing the resistance offered by the device [4]. This device is capable of up to 300 lbs. of force and can support all muscle groups in the human body.

Figure 8: Interim Resistive Exercise Device (iRED)

Ways of training the cardiovascular system on the international space station include the use of the Treadmill with Vibration Isolation and Stabilization (TVIS) system [11]. On the ISS, the TVIS is suspended within an opening in the service module floor and allows limited movement in six degrees of motion. The Vibration Isolation and Stabilization (VIS) System is intended to minimize the dynamic forces of exercise being transferred to the structure of the ISS service module, while maintaining a relatively stable exercise surface. Movement of the TVIS is counteracted with active (gyroscope and stabilizer) and passive (bungees and wire ropes) vibration isolation systems. The active components of the VIS system are the gyroscope, four linear slide-mass stabilizers, four motor controllers and a VIS controller. The running surface of the treadmill is used in much the same way as any conventional treadmill, except the user is held to its surface by the Series Bungee Systems (SBS), which uses latex rubber tubes and/or by the Subject Load Device (SLD), which attach to a shoulder and waist treadmill harness to counter the micro-gravity (μg) environ-

ment. When used without the SLDs, the SBSs are considered the contingency loading configuration [14].

Figure 9: Treadmill with Vibration Isolation and Stabilization (TVIS)

The second way of cardiovascular training in space uses the Cycle Ergometer with Vibration Isolation and Stabilization (CEVIS) system. The system is essentially a recumbent bicycle. CEVIS is computer controlled and maintains an accurate workload independent of pedal speed. The ergometer contains the main mechanics and electronics. Friction and resistance are applied to an internal flywheel via a braking band, which is adjusted by a stepper motor. The stepper motor adjusts the tension in the braking band to maintain a constant workload independent of pedal speed [23].

Figure 10: Cycle Ergometer with Vibration Isolation and Stabilization (CEVIS)

As described in the above examples, none of the current or former ISS exercise machines use electric motors to produce dynamic resistance. The CSU 4OptimX provides a conceptual platform for the development of space exercise machines such as the ARED and the iRED. A concept that will advance dynamically controlled exercise machines is presented in the next section.

1.2.3 Muscle Activation Feedback

Impedance control is fundamental and essential for human/machine interaction. Successful implementation of impedance control techniques involve the use of a force sensor to quantify the amount of human interaction with the robot. That interaction quantification is used by the controller for increased accuracy in obtaining the desired impedance. Elaborating further, it is a goal of many researchers in human/machine interaction to provide a bridge of data directly from the user to the

robot in order to allow for more advanced impedance control of robots. That bridge is muscle activation sensing through surface electromyography (sEMG). Li et al. uses these biological signals to design the optimal reference impedance model that allows an exoskeleton to supply the correct amount of impedance to the user [9].

Figure 11: Upper Limb Robotic Exoskeleton Using Biological Signals [9]

Developing an electro-skeletal model of the human upper limb and calibrating it to match the users motion behavior allows for this type of advanced impedance control to happen. More similar work done by Kiguchi et al. involves the same goal of advanced impedance control for exoskeletons using neural networks for optimal reference impedance determination [7].
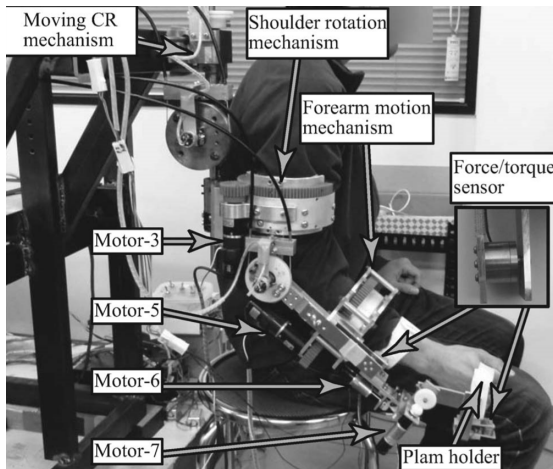
(a) Mechanism
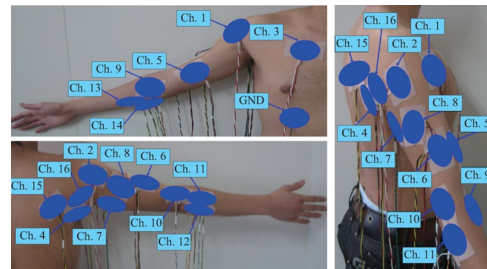
(b) EMG Placement

Figure 12: Upper-Limb Power-assist Exoskeleton Robot [7]

Song et al. also conducted successful research using EMG aided impedance

control to assist stroke patients during rehabilitation [22]. All of these examples apply to either robotic arms or exoskeletons that assist severely disabled users while they regain strength and mobility. Work toward exercise machines for advanced training or space applications using these concepts and ideas is sparse or non-existent based on extensive background research. It is in this thesis where the literature toward the previously stated idea will advance the next generation of exercise machines for a multitude of applications.

1.3   Mechanical Design

The CSU 4OptimX robot is a four degree of freedom, upper body exercise robot. It was designed and built by Funk Engineering under the specifications set forth by CSU researchers in human-machine systems. The robot consists of two arms that are independent of one another. Each arm allows for movement in two degrees of freedom (vertical, horizontal, and any orientation combination of the two) about a fixed pivot point. Each degree of freedom of each arm is powered by an independent servomotor system. There are four servo motor systems in total. Encoders specific to each servo motor system measure the rotational position of the motors. Force sensors strategically mounted on the arms of the robot capture the impedance forces of the manipulator. Shown below is a picture of the robot.
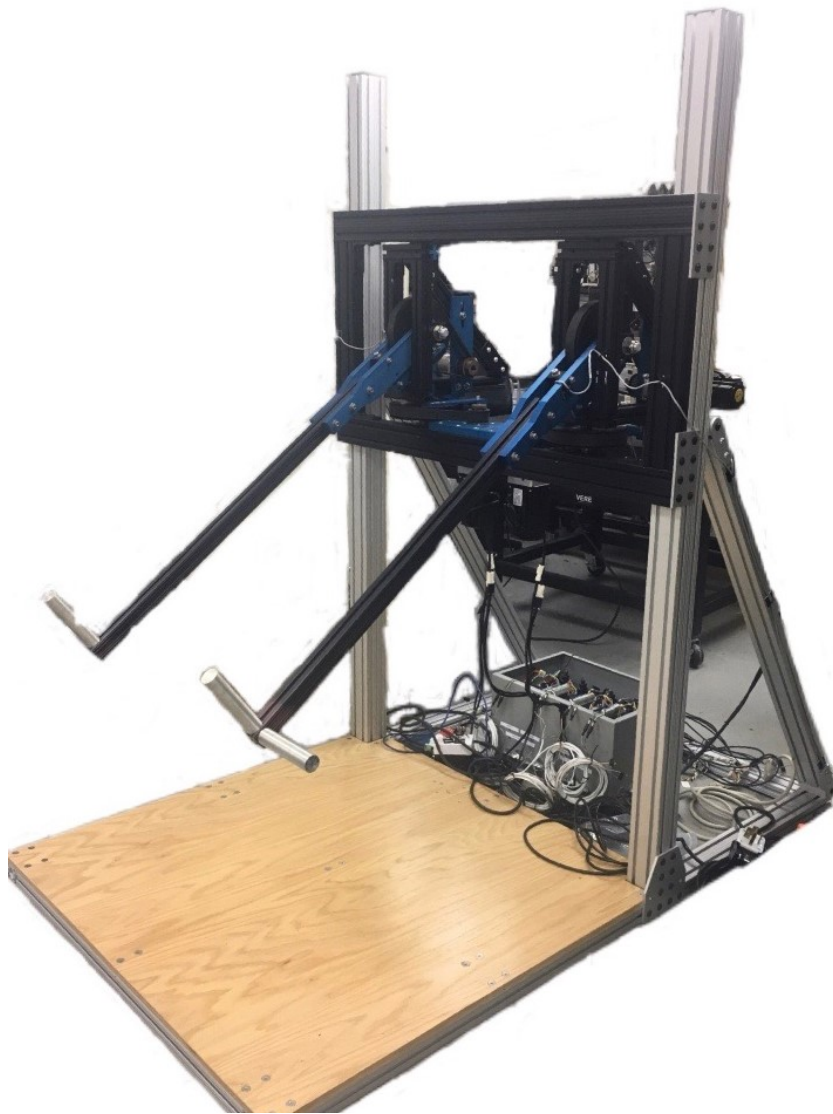
Figure 13: CSU 4OptimX Exercise Machine

The mechanical design of the robot for each degree of freedom is identical. Therefore, the description of the mechanical path from the motor to the force sensor is identical. The path begins at the motor. The motor is geared to produce a 25:1 ratio of motor rotations to output shaft rotations. Any variables with the subscript m hereafter refers to the geared output shaft of the motor, not the motor itself. The output shaft is attached to a sprocket/timing belt mechanical system that ultimately attaches directly to the arm. The gear ratio from the motor output shaft to the arm of

the robot is 3.858:1. Finally, a force sensor is mounted between the arm of the robot an a fixture attached to the large sprocket of the sprocket/timing belt mechanical system. This clever design allows for the large sprocket and the arm to be fixed in rotation together while allowing an external force on the arm to be measured in relation to the movement of the arm itself.

(a)

(b)
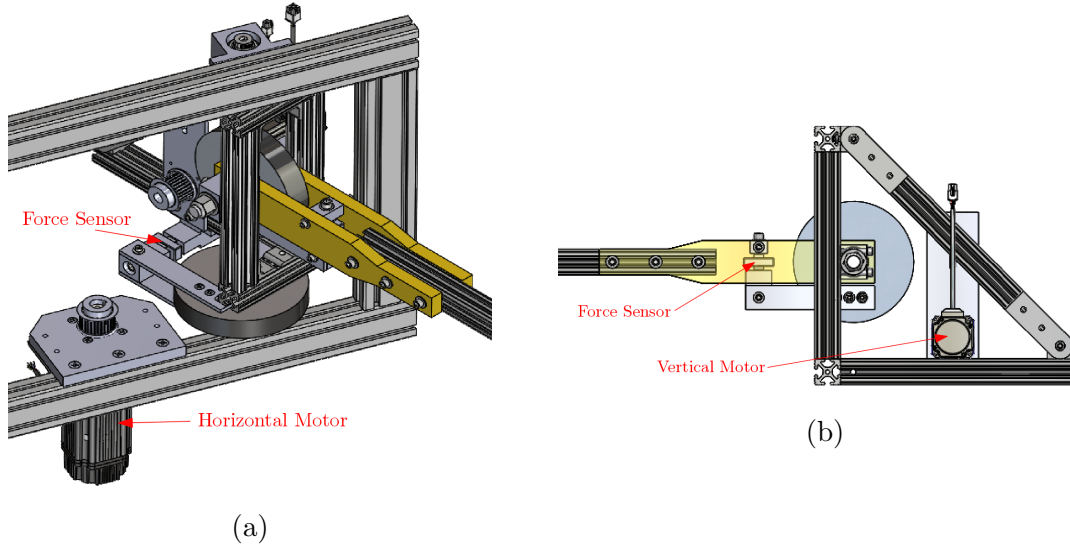
Figure 14: Detailed View of Exercise Machine

Four motors in total allow for the movement of the arms. The horizontal movement of each arm is powered by individual Estun PKS-PRO-E-08-B-JP22 servomotor systems. The vertical movement of each arm is powered by individual Estun PKS-PRO-E-04-A-JP22 servomotor systems. Below is table showing the parameter values for each servomotor system.

System	Rated Power (W)	Rated Voltage (VAC)	Rated Speed (RPM)	Rated Torque (N-cm)	Rated Current (A rms)	Brake	Shaft Diameter (mm)
PKS-PRO-E-08-B-JP22	750	85-132 Single Phase	3000	238.68	8.2	No	19
PKS-PRO-E-04-A-JP22	400	170-253 Single Phase	3000	127.11	2.7	No	14

Table I: Servomotor System Parameters

Speed versus torque curves are shown for each motor. Curve A represents the con-

tinuous working area while curve B represents the repeated working area.

(a) EMJ-08-B

(b) EMJ-04-A
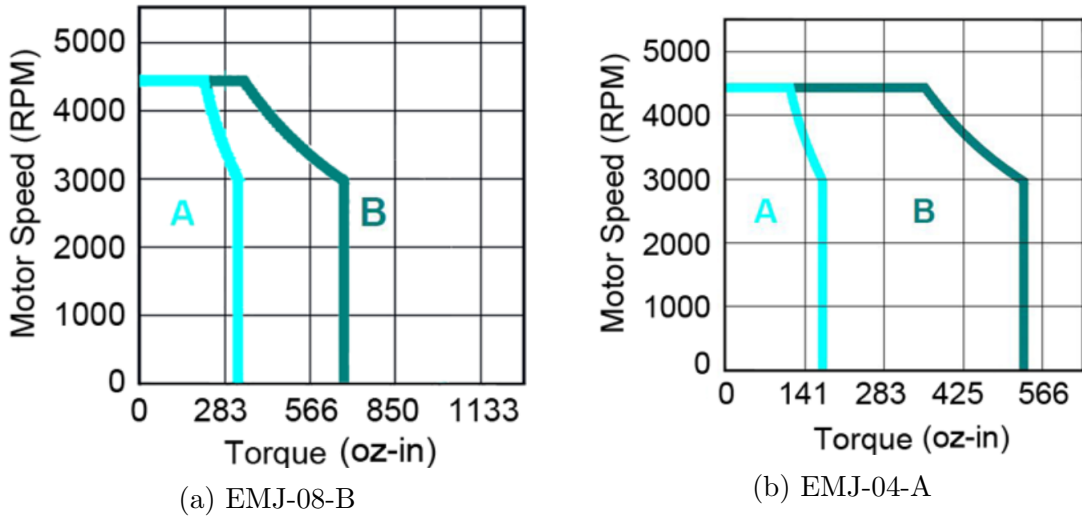
Figure 15: Motor Speed vs. Torque Curves

The servomotor systems are able to be operated in position, speed, or torque control. For this application, the servomotors are operated in torque control. Each servomotor has a 2500 pulse per revolution (PPR) incremental encoder for reading motor position. Similarly, four force sensors are mounted on the robot; two per arm and one per degree of freedom. The sensors are single axis, tension/compression force sensors distributed by Omega Engineering. The following table is the force sensor specifications.

LC703-500 Load Cell	
Material	17-4 PH Stainless Steel
Capacity (lbs)	500
Excitation (VDC)	10 (15 max)
Output (mV/V)	2
Max Deflection (in)	0.003

Table II: Force Sensor Specifications

Together, the described sensors and actuators make up a mechatronic system capable of being modeled and controlled.

The kinematics and dynamics of this exercise machine allow the user to perform a plethora of upper body exercise movements such as lat pull downs, shoulder

presses, pectoral flies, bicep curls, and triceps extensions to a challenging degree. The mechanical and electrical design goals of this robotic exercise machine are to enable a wide range of exercises using multiple muscle groups and to provide adequate muscle activation for control system feedback research. Listed below are end effector abilities.

Direction	Displacement (Rad)	Rated Force (N)	Rated Speed (RPM)
Vertical	+0.894, -0.627	108.49	31.1
Horizontal	+0.449, -0.235	203.72	31.1

Table III: End Effector Capabilities

Using data presented in Kulig et al., determining whether the exercise machine is capable of producing "adequate" muscle activation can be addressed [8]. Adequate muscle activation, as it pertains to this thesis and application, refers to the amount of muscle activation needed to see a variation in force production for a control system to use as feedback. A verified example of "adequate" muscle activation as a result of a conducted experiment will be presented later on in this thesis. Data presented in Kulig et al. is shown as force verses joint angle curves, or strength curves. Extracting maximum forces produces by shoulder and elbow joint torques will provide a reasonable quantification for comparing the input forces of the user to the output forces of the exercise machine end effector.
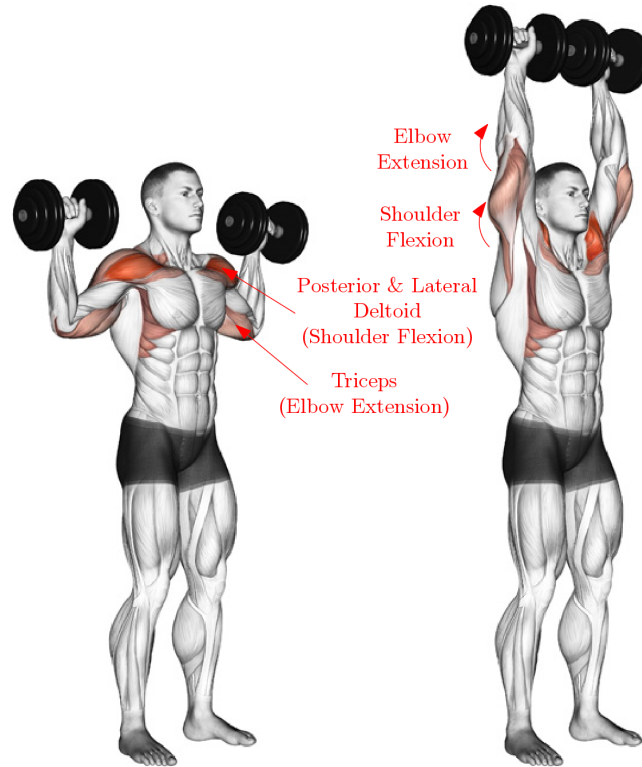
Figure 16: Shoulder Press Exercise

The amount of force at the hand generated during shoulder flexion in college males and females was found to be roughly 500 N and 225 N, respectively [8]. Comparatively to the exercise machine, college age males and females were able to produce 4.6 and 2.0 times the force able to be produced by motor 1 of the exercise machine. Shoulder flexion is the main movement in a general shoulder press gym exercise and is a vertical movement. For that reason, motor 1 was chosen for the comparison. For research purposes, the largest possible amount of muscle activation is preferred. College age males and females are able to generate 200 N and 140 N during elbow extension, which also occurs in a shoulder press movement [8]. Comparatively, they are generating 1.85 and 1.3 times the force that motor 1 of the exercise machine can produce. Similar to shoulder flexion, the exercise machine is capable of producing forces nearing the maximum force of elbow extension in women.

Comparing the data in the literature with the capabilities of the robot end

effector, it is not immediately evident that the robots end effector force capacity is large enough to produce adequate muscle activation. Notably, this machine was built for experimentation purposes. It was not intended to supply a larger end effector force than the user can manage. Its purpose is to produce adequate muscle activation, as defined earlier. In order to verify that the machine is capable of inducing adequate muscle stimulation, an experiment was done on this machine using a male subject.

1.3.1   Muscle Activation Verification Experiment

The experiment consisted of the male subject attempting to follow a predefined, circular trajectory with the arm of the robot while his muscle activation in multiple upper body muscles is measured. For clarity, a figure of the visual interface the subject used the follow the trajectory is shown below.
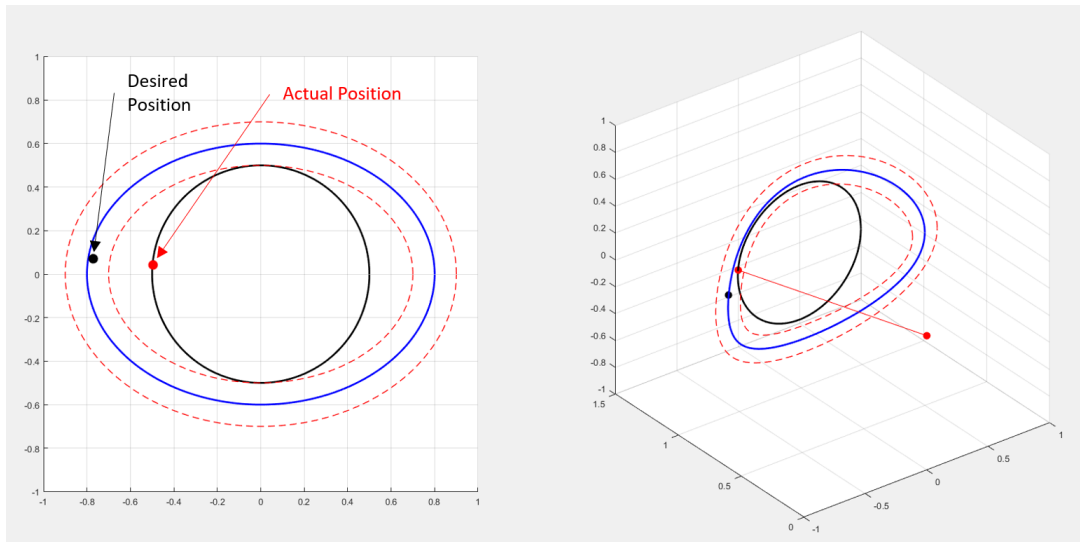
Figure 17: User Interface for Muscle Activation Experiment

The black circle is what can be referred to as the zero impedance trajectory. If the user is in phase with the desired position and on the zero impedance trajectory, the user will feel no impedance force imposed by the robot. When the user deviates in any direction from that zero impedance trajectory or becomes out of phase with the

desired position, an impedance force will be felt by the user. Using this concept, the subject was told to follow the desired position as it travels around the blue ellipse. This intentional deviation causes upper body muscle activation, which is then measured by electromyography (EMG) sensors. This procedure was done using different robot impedance parameters and circular trajectory speeds. A portion of the data gathered from this experiment is shown below.
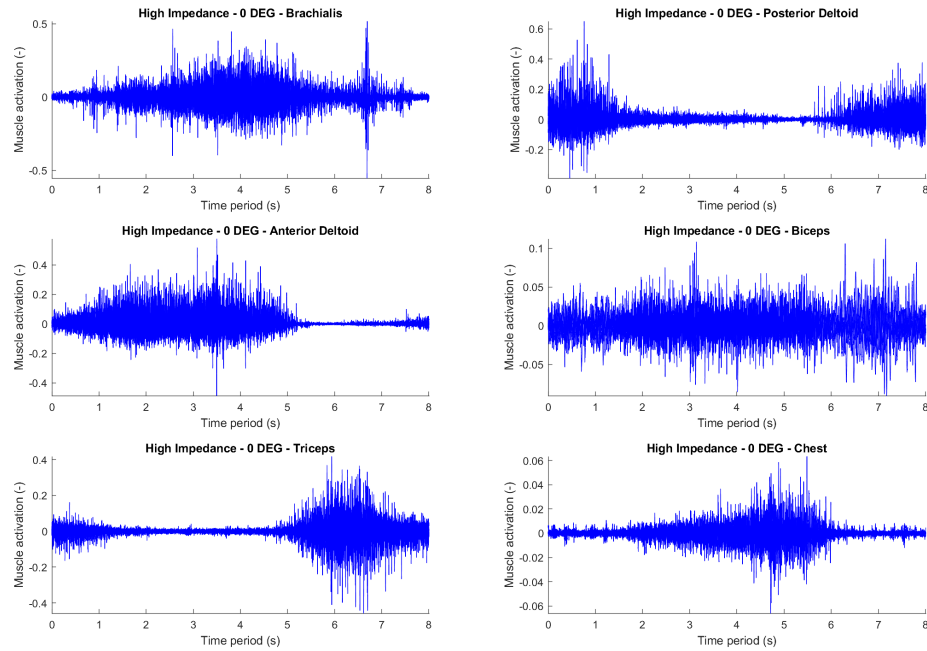
Figure 18: Muscle Activation Experimental Results

As is evident, there are significant spikes in muscle activation for the period of rotation. Various muscles record activation spikes at different times during the period of rotation, which is also a very promising result. This experiment verifies the ability of the CSU 4OptimX to produce enough impedance force to significantly activate various muscles of the male user.

1.4   Organization

In order to represent the methods used in this thesis and the results obtained from them, a thorough review of the background material is presented at the beginning of every chapter. If applicable, an simple example of the theory being implemented is shown next. The theory will then be implemented toward the goal of this thesis. The chapters follow the flow of the control design procedure. In Chapter 2, the nominal and uncertain plant is mathematically modeled and its parameters identified. In Chapter 3, the nominal and uncertain plant is used in the sliding mode and $\mathcal{H}_\infty$ robust control lows to synthesize respective controllers. Chapter 4 presents and explains the results pertaining to the performance, robustness, and practicality of each synthesized controller. Finally, concluding remarks comparing the success of each controller and the limitations in the control laws observed during synthesis are discussed in Chapter 5. Future work pertaining to the possibility of increased success with select control laws is also explained.

CHAPTER II

Modeling and Identification

This chapter begins with a description of the physical model of the plant. From that physical model, first order transfer functions are obtained that describe the input-output behavior of the CSU 4OptimX. System identification is then explained and performed to find parameter values for the nominal transfer function variables. The $\mathcal{H}_\infty$ robust control law implemented in this thesis uses an uncertain plant description to synthesize a controller. The theory behind various uncertain plant descriptions is elaborated upon at the end of the chapter.

2.1 Physical Modeling

Each joint was modeled independently. Inertial coupling between the joints was ignored to maintain simplicity. The modeling assumption is justified due to the low operating speeds of the joints. Beginning with the servo motor, the modeling of the plant will capture the dynamics all of the way through to the force sensor on the arm of the robot. The plant will be assumed to have no gravitational forces acting on the arm. Forces due to gravity will be compensated via a control loop during controller implementation. This assumption allows the dynamic equation to be linear and therefore easier to implement the control laws. The goal will be to find a first

order linear differential equation that describes the CSU 4OptimX robot.

Traditional modeling techniques require the creation of a free body diagram. As stated earlier, this free body diagram will show the single plane dynamics of one of the robot arms.
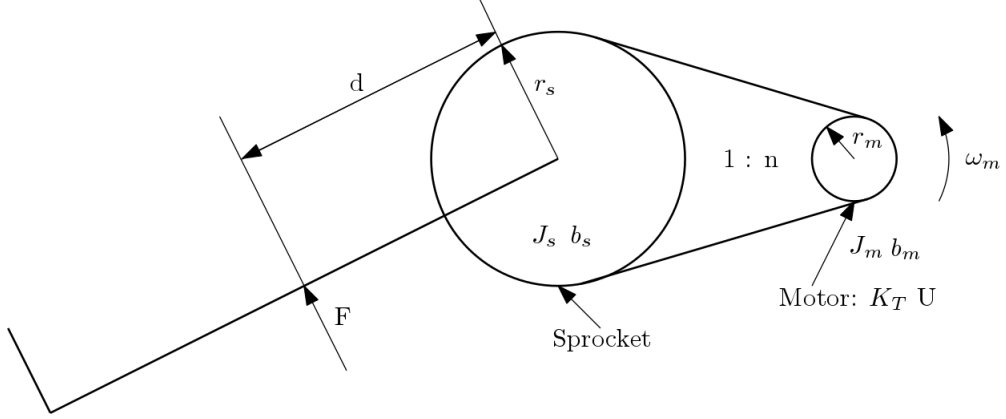
Figure 19: Schematic of Single Plane Dynamics

A linear first order differential equation of the servo motor is where the analysis begins.

$$J_m \dot{\omega}_m + b_m \omega_m = K_T U - T_L \tag{2.1}$$

J_m is the rotational inertia of the motor, b_m is the rotational damping of the motor, $\dot{\omega}_m$ is the angular acceleration of the motor, ω_m is the rotational velocity of the motor, K_T is the torque voltage constant, U is the control voltage, and T_L is load torque on the motor. Inductive and resistive dynamic effects were not modeled since torque control was chosen for this application. Those effects are only modeled in applications involving speed control. Examining electric servomotor equations will verify this claim. The load torque of the motor due to the arm and imposed impedance force can be modeled as such.

$$T_L = \frac{J_s \dot{\omega}_s + b_s \omega_s + dF}{n} \tag{2.2}$$

J_s is the sprocket rotational inertia, $\dot{\omega}_s$ is the angular acceleration of the sprocket, b_s is the rotational damping of the sprocket, ω_s is the angular velocity of the sprocket, d

24

is the moment arm length from the pivot point of the sprocket to the load sensor, F is the load sensor force, and n is the gear ratio between the motor and the sprocket. Combining equations (2.1) and (2.2) yields the following linear first order differential equation describing the dynamics of one degree of freedom of the CSU 4OptimX robot.

$$J_T \dot{\omega}_m + b_T \omega_m = K_T U - ndF \tag{2.3}$$

where J_T and b_T given by the following equations:

$$J_T = J_m n^2 + J_s \tag{2.4}$$

$$b_T = b_m n^2 + b_s \tag{2.5}$$

Equations (2.4) and (2.5) represent the inertial and damping effects of the motor and gears reflected to the arm. These relations will be denoted as the total rotational inertia and damping of the plant. The respective transfer functions are the following:

$$\frac{\omega_m(s)}{U(s)} = \frac{K_T}{J_T s + b_T}, \quad \frac{\omega_m(s)}{F(s)} = \frac{nd}{J_T s + b_T} \tag{2.6}$$

As a summary, this plant model can be applied to each degree of freedom for each arm as the mechanics of the modeled arm for each degree of freedom is identical. It is evident in the equations that the effects of gravity on the arm were not modeled. Those effects were treated separately using a compensation control loop in application.

2.2 Modeling by System Identification

System identification is a methodology for building mathematical models of dynamic systems using measurements of the system's input and output signals. The

process of system identification requires that the designer:

- Measure the input and output signals from a system in time or frequency domain

- Select a model structure.

- Apply an estimation method to estimate value for the adjustable parameters in the proposed model structure.

- Evaluate the estimated model to see if the model is adequate for your application needs.

System identification can be done using black-box or grey box modeling structures. Black-box modeling does not specify a detailed, parametric structure of the system that the data attempts to fit. Black-box modeling is useful when the primary interest is in fitting the data regardless of a particular parametric structure of the model.

Input → **BLACK BOX** → Output
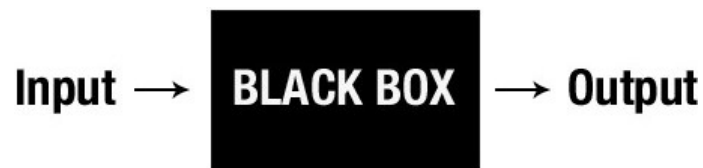
Figure 20: Black-Box System Identification

Grey-box modeling specifies a detailed, parametric structure of a physical system that the data attempts to fit. In situations where the theoretical mathematical model of the physical system can be found, grey-box modeling fits the input-output data to that particular model by finding the exact parameters of that model.
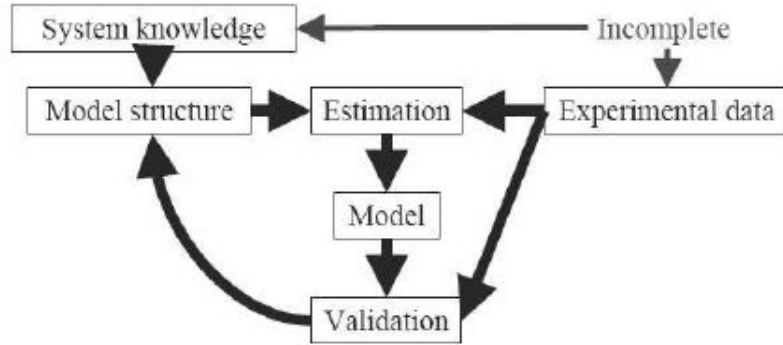
Figure 21: Grey Box System Identification

2.2.1 Nominal Plant

The parameter identification any system involves exciting all frequencies of the system that will occur during operation. For the nominal plant of the CSU 4OptimX, a general frequency range of 0-125 $\frac{rad}{s}$ was chosen as the general opertaiong bandwidth of the system. In order to excite the bandwidth frequencies, a random input signal was chosen for this application due to its ability to create unstructured inputs that produce varying frequencies. In this application, a force sensor will produce random inputs to the system. Therefore, it is advantageous to use a random input when identifying the system. Input-output data is gathered for input into the MATLAB System Identification toolbox.

The input-output data is used to fit the following first order transfer function.

$$G_1(s) = \frac{K_T}{J_T s + b_T} \tag{2.7}$$

The first order transfer function is the mathematical model of the physical system presented below.
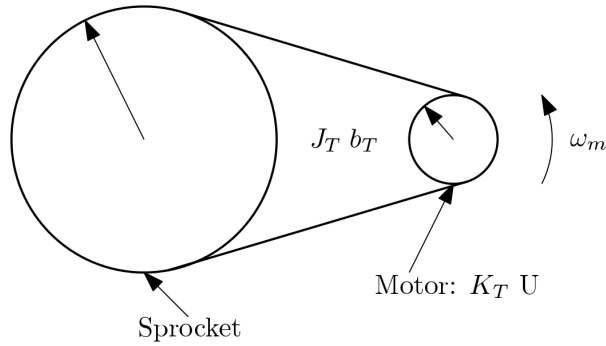
Figure 22: Parameter Identification Physical Model

Using MATLAB and the function `ident` brings up the System Identification Toolbox. This toolbox is a powerful tool for estimating the parameters of a grey-box or black-box system. For this parameter identification, black-box identification was used to fit a first order transfer function with one pole and no zeros. Black-box system identification was used due to its ability to better fit the transfer function structure. Even though a plant structure is specified, the plant structure is simple enough to back calculate the parameter values from the specified black-box transfer function. Firstly, the input/output data must be frequency filtered. This is done so that a preferred frequency range can be chosen for the identification. It is advantageous to limit the bandwidth of the identification data to the expected bandwidth of operation in order to produce optimally fitting parameters. It is also beneficial to remove means and trends in the data. Using this filtered data and specifying the transfer function as a first order transfer function consisting of only one pole and no zeros, a statistical fit done by the toolbox estimates the coefficients of the transfer function. MATLAB shows the fitted transfer function in the following form.

$$TF(s) = \frac{\frac{K}{J}}{s + \frac{B}{J}} \tag{2.8}$$

Separate from the system identification, a static hold test must be conducted to determine the voltage/torque relation, K_T, for future use in comparing the MAT-

LAB results of the system identification presented by (2.8) with the user-defined function (2.7). The principle of a static hold test is to determine the amount of torque per volt needed to maintain the arm of the robot at its maximum inertial position without movement. That position is parallel with the ground. The associated equation for testing is shown below.

$$K_T U - ndF = 0 \qquad (2.9)$$

This equation can be solved for K_T knowing values of U and F obtained in testing. Comparing the MATLAB results of the respective mechanical systems in the form of (2.8) to equation (2.7) will yield the coefficients J_T, b_T.

2.2.2 Uncertain Plant

In order to extract the benefits from controllers synthesized using robust control techniques, it is necessary to model the amount of uncertainty present in the parameters of the plant. Alternatively, if the amount of parametric uncertainty is not known, un-modeled dynamics of any form can be included as information to the robust controller synthesis algorithms. Factoring in parametric uncertainty or un-modeled dynamics gives the controller increased knowledge of the possible variations of plants it may be controlling. This will directly increase controller performance and robustness. There are different methods in which to model unknown information within a control system. The three explained in this thesis will be structured parametric uncertainty, additive model error, and multiplicative model error.

2.2.2.1 Structured Parametric Uncertainty

Parametric uncertainty is the idea that the variables of a plant model vary in a range, either statically or dynamically, over a range of frequencies. It is struc-

tured because the variations in plant output can be precisely described in terms of corresponding variations of the parameters. Identifying and modeling this parameter variation is essential to understanding the capabilities of a plant in order to synthesize a controller to manipulate it. Initially, a nominal model of a plant using nominal parameters can be found using methods in Section 2.2.1. Intuitively, it is understood that this nominal plant model is not representative of the true dynamics of the plant for many reasons. Therefore, nominal variables in a plant can be modified to include uncertainty in their values. For example, using the plant in Figure 1a, an uncertain mass parameter can be described by the equation below.

$$m = m_o + W_m(s)\Delta \tag{2.10}$$

x_m is the nominal mass value, $W_m(s)$ is a weight that shapes the variation in the magnitude of the mass of the parameter over a frequency range, and Δ is the normalized uncertainty where $||\Delta||_\infty \leq 1$. The left hand side of the inequality is the $\mathcal{H}_\infty$ norm of the uncertain dynamics. The $\mathcal{H}_\infty$ norm is simply the peak value of a frequency function (i.e. transfer function).

$$||f(s)||_\infty \triangleq \max |f(j\omega)| \tag{2.11}$$

Normalized uncertainty can be expressed in MATLAB using the `ultidyn` function. This uncertain equation can then be combined with the plant dynamics.

$$m_o\ddot{x} + W_m(s)\Delta\ddot{x} = F_A - F_P \tag{2.12}$$

The idea of un-modeled dynamics and its association with parametric uncertainty becomes increasingly clear when represented in a block diagram.
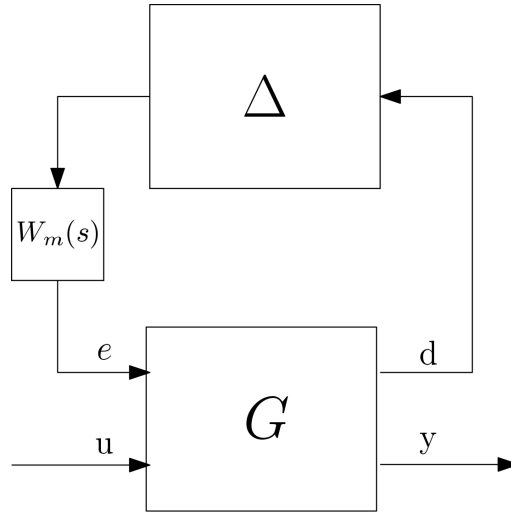
Figure 23: General Structured Parametric Uncertainty

Variable d represents the acceleration of the mass, $\ddot{x}$, variable e represents $W_m\Delta\ddot{x}$, which is the mass uncertainty dynamics that are added to the nominal mass, m_o. This concept can be more clearly explained using a detailed block diagram.
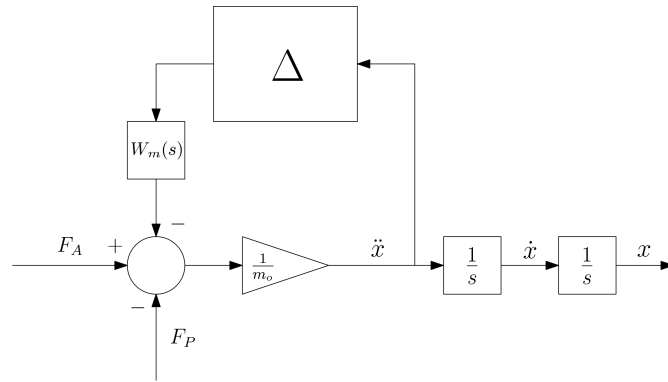
Figure 24: Detailed Structured Parametric Uncertainty Example

This method of bounding the uncertainty in plant parameters is important when synthesizing an $\mathcal{H}_\infty$ controller. The details of $\mathcal{H}_\infty$ controller synthesis will be discussed in the next chapter.

2.2.2.2   Additive Model Uncertainty

Model uncertainty is a discrepancy in the dynamics of a model between the nominal, experimentally-modeled dynamics and the true dynamics of the system. Normally, this discrepancy is within a specified frequency range instead of over the entire operating frequency range of the system. This gap in modeled dynamics is commonly known as the un-modeled dynamics of a system. In the previous section, structured uncertainties in the parameters of the plant are addressed. That method can be considered a more detailed description of system uncertainty due to the designer having knowledge of the range of plant parameters though out the frequency range of the system. Model uncertainty is more vague. It is the idea that there is uncertainty in the system, but a definite structure cannot be defined. This is known as unstructured uncertainty.

Unstructured uncertainty can be expressed additively within a plant. Additive model uncertainty is the absolute error between the true plant and the nominal plant. Generally, system block diagrams factoring in additive uncertainty take the form of the figure below.
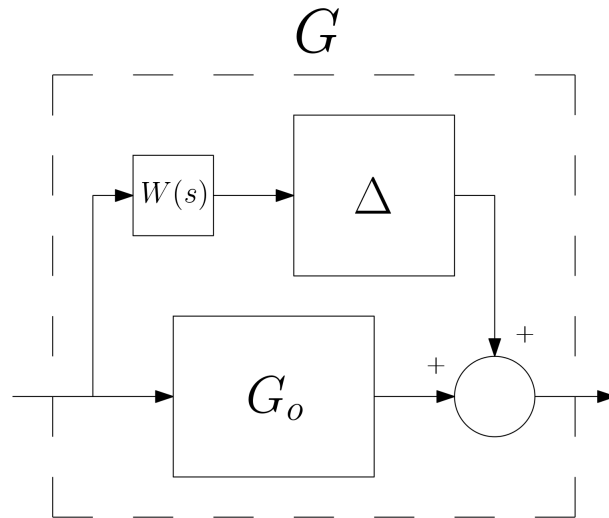
Figure 25: Additive Model Uncertainty

Additive model uncertainty is expressed as the difference between the true plant, G,

and the nominal plant, G_o.

$$W(s)\Delta = G - G_o \tag{2.13}$$

$W(s)$ is a weight that shapes the amount of unmodeled dynamic uncertainty through a frequency range. The weight shape must satisfy the following equation:

$$|\Delta_i(j\omega)| = |G_i(j\omega) - G(j\omega)| \leq |W(j\omega)| \tag{2.14}$$

where Δ is the normalized uncertainty where $||\Delta||_\infty \leq 1$. $G_i(i = 1, 2, ...)$ are a number of identified plants that have varying errors from the true plant, G. This equation means that the weighting function used to shape the error must be less than or equal to the iterative error found through identification and comparison. Practically, the true dynamics of the plant can never be known fully. Typically, the nominal plant model is used as the true plant model and any other plant models found through system identification can be used as iterative plant models, pertaining to equation (2.14). Using this practical method, a plant modeling error is produced and a weight can be shaped that describes this modeling error. The final description of additive modeling error is similar to structured parametric uncertainty but at a plant level and not a parameter level.

$$G = G_o + W(s)\Delta \tag{2.15}$$

2.2.2.3   Multiplicative Model Uncertainty

Multiplicative model uncertainty is similar to additive uncertainty in the sense that it is the discrepancy between the unmodeled dynamics of the true plant and nominal plant, but, instead of the error being absolute, the error is now relative to the nominal plant model. A block diagram representing multiplicative uncertainty is shown below.
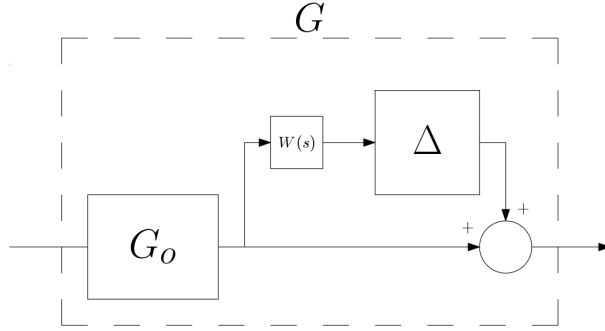
Figure 26: Multiplicative Model Uncertainty

The relative error can be found by the following equation:

$$W(s)\Delta = \frac{G - G_o}{G_o} \tag{2.16}$$

where Δ is the normalized uncertainty where $||\Delta||_\infty \leq 1$. Normalized uncertainty can be expressed in MATLAB using the `ultidyn` funciton. G_o is the nominal plant model and G is the true plant model. W(s) is a weight that shapes the amount of unmodeled dynamic uncertainty through a frequency range. The weight shape must satisfy the following equation:

$$|\Delta_i(j\omega)| = \left|\frac{G_i(j\omega) - G(j\omega)}{G(j\omega)}\right| \leq |W(j\omega)| \tag{2.17}$$

where $G_i(i = 1, 2, ...)$ are a number of identified plants that have varying errors from the true plant, G. This equation means that the weighting function used to shape the error must be less than or equal to all errors found through system identification. Practically, the true dynamics of the plant can never be fully known. Typically, the nominal plant model is used as the true plant model and any other plant models found through system identification can be used as the iterative plant models, pertaining to equation (2.17). Using this practical method, a plant modeling error is produced and a weight can be shaped that describes relative modeling error. The final description

of multiplicative modeling error is shown below.

$$G = (1 + W(s)\Delta)G_o \tag{2.18}$$

CHAPTER III

Robust Control

Robust control is a group of control laws that explicitly deal with plant uncertainties, whether they are structured or unstructured, and disturbances. For many physical systems, determining accurate plant parameters and disturbances models is challenging or even infeasible. By quantifying the uncertainty in plant parameters and disturbances, a controller with increased performance is able to be obtained. Due to the parameter identification errors (friction and disturbance anomalies evident in the motor input signals), robust control was chosen as a viable solution to properly controlling the CSU 4OptimX.

The controllers in this chapter are designed under the following assumptions:

- Each joint will be independently controlled.

- A controller will be designed for each joint.

- Gravity will be compensated for the vertical joints by an independent control loop.

Two robust methods are chosen for this application: sliding mode control and $\mathcal{H}_\infty$ control. In this chapter, an outline of the theory will be presented first. Then an elementary example that applies the theory to impedance control is explained in

detail. Finally, the controller design for the CSU 4OptimX is incrementally explained as well as the minor modifications to the theory that allow a practical controller to be synthesized.

3.1 Sliding Mode Control

The first type of control implemented on the CSU 4OptimX robot is sliding mode control. By nature, it is less abstract and computationally intensive than other advanced control techniques. It proves to be a sufficient introductory impedance control for this robot and for the engineer developing it. Much of the theory and design of this sliding mode impedance controller is referenced from Advanced Control of Turbofan Engines by Dr. Hanz Richter [19] and Advanced Sliding Mode Control for Mechanical Systems: Design, Analysis and MATLAB Simulation by Jinkun Liu and Xinhau Wang [10]. Discussed in this section will be the background theory describing sliding mode control, a simple example that shows how to use sliding mode control to regulate impedance, and the impedance/sliding mode controller design as is pertains to the CSU 4OptimX exercise machine.

3.1.1 Theory

Sliding mode control (SMC) is a branch of non-linear robust control techniques that has become popular due to its insensitivity to plant uncertainties and remarkable disturbance rejection capabilities. The controller operates on a general, non-linear, switching function called a reaching law.

$$\dot{s} = -\eta sgn(s) - f(s), \quad \eta > 0 \tag{3.1}$$

The purpose of this reaching law is to drive a sliding function, s, to zero and keep that function within predetermined bounds around zero. It is important that the sliding function is driven to zero because it generally represents the error. In the majority of control applications, minimizing the error between two variables is the goal. The general reaching law is presented above in (3.1). The signum function is a non-linear function that switches instantaneously from $sgn(s) = -1$ if $s < 0$ and $sgn(s) = 1$ if $s > 0$. Common reaching laws implemented in practice are specified in Table IV.

Name	Function ($\dot{s}$)	Specification
Constant Rate	$-\eta sgn(s)$	$\eta > 0$
Exponential	$-\eta sgn(s) - ks$	$\eta > 0, \quad k > 0$
Power Rate	$-k|s|^{\alpha} sgn(s)$	$k > 0, \quad 1 > \alpha > 0$

Table IV: Sliding Mode Reaching Laws [10]

The zero line on a time plot in SMC is referred to as the sliding surface.

The sliding function, s, must reach the sliding surface ($s = 0$) in finite time and remain on the sliding surface in order to achieve the goal, which is the sliding function. An example of the sliding surface is shown in Figure 27.
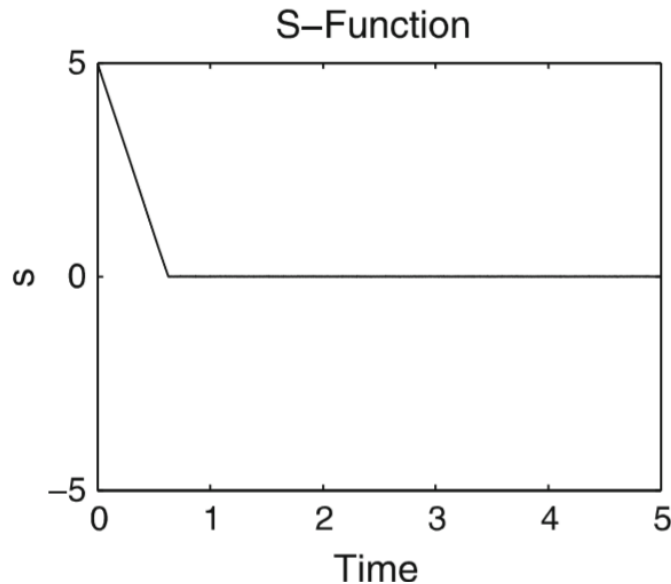
Figure 27: Sliding Function Reaching the Sliding Surface

The sliding function, s, allows one state variable to be represented in terms of one

or more state variables. When it is combined with the plant model later on in the design, the order of the system is reduced. In order to ensure that the sliding function will reach the sliding surface from any direction, the switching and sliding functions must satisfy equation (3.2) for $s < 0$ and $s > 0$.

$$s\dot{s} < 0 \qquad (3.2)$$

Combining a preferred reaching law with the inverse dynamics of the plant to produce the controller is a design and implementation problem. It will be discussed in the next section.

3.1.2 Example

The following is a conceptual example that will show how to correctly apply SMC theory to impedance control. This example will use the physical and mathematical plant description shown in Figure 1a and equation (1.2). Also, the same impedance relation shown in (1.3) will be used as the sliding function, s, and shown in (3.3).

$$s = M\ddot{x} + B\dot{x} + Kx + F_P = 0 \qquad (3.3)$$

Next, a reaching law will be chosen that will force the sliding function to the sliding surface, $s = 0$. The reaching law chosen for this example will be the constant rate reaching law found in the second row of Table IV. In order to verify that the function will reach and remain on the sliding surface, it must satisfy (3.2).

$$s\dot{s} = -\eta \, sgn(s)(M\ddot{x} + B\dot{x} + Kx + F_P) < 0 \qquad (3.4)$$

If $s > 0$, $sgn(s) = 1$ and $\dot{s} < 0$, therefore $s\dot{s} < 0$. If $s < 0$, $sgn(s) = -1$ and $\dot{s} > 0$, therefore, $s\dot{s} < 0$. The reaching law can now be combined with (1.3) in the following

manner.

$$M\ddot{x} + B\dot{x} + Kx = -F_p - \eta sgn(s) \tag{3.5}$$

This equation shows that the force of all impedance components must be equal to the opposite of the applied force of the person pushing on the mass minus the reaching law. The reaching law forces the impedance force and the applied force of the person to be equal to a small degree of error. Perfect impedance with sliding mode is not achievable. What is achievable is near perfect impedance within a boundary layer condition presented in Section 3.1.1. Next, as shown in (1.4) for the simple impedance example, equations (3.5) and (1.2) can be solved for their accelerations and combined as shown in (3.6).

$$\frac{F_A - F_P}{m} = -\frac{\eta sgn(s) + F_P + Kx + B\dot{x}}{M} \tag{3.6}$$

Finally, the above equation can be solved for the actuator force, F_A. The controller equation is shown below.

$$F_A = -\frac{m}{M}\eta sgn(s) + \left(1 - \frac{m}{M}\right)F_P - \frac{mK}{M}x - \frac{mB}{M}\dot{x} \tag{3.7}$$

3.1.3 Controller Design

Using the sliding mode control theory established in Section 3.1.1, an SMC impedance controller is formulated for the CSU 4OptimX exercise machine. Reiterating, each motor will have its own controller. Therefore each plane of motion will have its own controller. These controllers act independent of each other. The controller designed hereafter is suitable for each plane of motion of the robot and can be implemented directly without modification.

Initially, a target behavior must be established and is represented below.

$$I(\dot{\omega}_m - \dot{\omega}_d) + B(\omega_m - \omega_d) + K(\theta_m - \theta_d) = -ndF \tag{3.8}$$

From the target behavior, a sliding surface is determined. The sliding function for the CSU 4OptimX is the following function.

$$s = \int I(\dot{\omega}_m - \dot{\omega}_d) + B(\omega_m(t) - \omega_d) + K(\theta_m - \theta_d) + ndF \ dt = 0 \qquad (3.9)$$

Variables with subscript d represent desired tracking variables acceleration, velocity, and position. This use of the integral in the sliding function is called impulse-momentum SMC. It becomes necessary to take the integral of the impedance function to obtain a relative degree of one between the sliding surface and the impedance function. When taking the derivative of the integral of the sliding surface, s, the impedance equation is the result and is equal to $\dot{s}$. It can then be set equal to the reaching function, which is also $\dot{s}$.

Using impulse-momentum SMC aids the practical implementation of this controller as well. Theoretically, acceleration can be calculated in simulation but not in practice. In simulation, measurements are ideal, meaning measurement noise is not present. In practice, measurement noise is present and prevents the application of more than one derivative to a signal. In some cases, even one derivative is challenging to compute the amplification of noise. Shown below is an example of measurement noise.
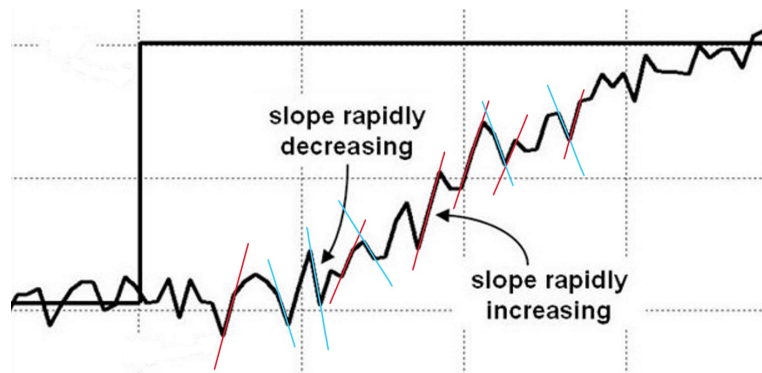
Figure 28: Measurement Noise Example

Red lines represent positive slopes and blue lines represent negative slopes. As is

evident, the slopes of this signal at different points in time vary greatly and does not represent the true slope of this line at different points in time. If the individual slopes represented in Figure 28 were plotted in time, only noise would be present.

Due to the noise amplification phenomenon of derivatives, motor acceleration, $\dot{\omega}_m$, cannot be obtained from the measured motor position, θ_m, in practice. Taking the integral of the sliding function does not change the integrity of the difference relation present in the function. Using this integral, $\dot{\omega}_m$ can be integrated to ω_m.

$$s = I\omega_m + \int -I\dot{\omega}_d + B(\omega_m - \omega_d) + K(\theta_m - \theta_d) + ndF \ dt = 0 \qquad (3.10)$$

The constant rate reaching law is incorporated with (3.8).

$$I(\dot{\omega}_m - \dot{\omega}_d) + B(\omega_m - \omega_d) + K(\theta_m - \theta_d) = -ndF - \eta sgn(s) \qquad (3.11)$$

Finally, to produce a controller, equations (2.3) and (3.11) must each be solved for $\dot{\omega}_m$, combined, and solved for the input control voltage, U. This produces a sliding mode controller that uses a target behavior, the control theory, and the inverse dynamics of the plant to ultimately control the behavior of the arm to an applied force.

$$\begin{aligned}
U = -\frac{J_T}{IK_T}\eta sgn(s) + \left[\frac{b_T}{K_T} - \frac{BJ_T}{IK_T}\right]\omega_m - \frac{KJ_T}{IK_T}\theta_m + \frac{KJ_T}{IK_T}\theta_d + \frac{BJ_T}{IK_T}\omega_d \\
+ \frac{J_T}{K_T}\dot{\omega}_d + \left[\frac{nd}{K_T} - \frac{ndJ_T}{IK_T}\right]F
\end{aligned} \qquad (3.12)$$

For implementation purposes, it is not practical to use a signum function. Avoiding its use will prevent against instantaneous switching in the control input, called chatter. If chatter is large or constant in the input, it will induce extra wear on the motor, changing its dynamics over time. It is common practice to approximate the switching function as a saturation function, $sat(\frac{s}{\phi})$, with a boundary layer, ϕ.

(a) Signum Function   (b) Saturation Function
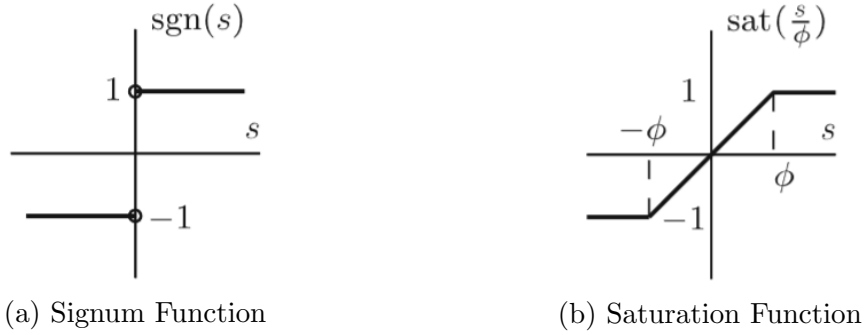
Figure 29: Signum vs. Saturation Function Representation [19]

This resolution will allow for a gradual switching between $\pm\phi$ when close to the sliding surface and prevent chatter in the motor. Simulink implementation of $\eta sat(\frac{s}{\phi})$ is shown below. The minimum and maximum values when specifying the saturation function are -1 and 1.
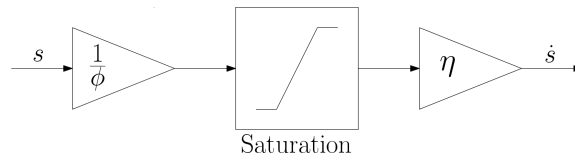
Figure 30: Reaching Function Practical Implementation in Simulink

A SMC impedance controller has been synthesized for one degree of freedom in the CSU 4OptimX robot. This control design process is identical for all 4 degrees of freedom given specific motor parameters for each degree of freedom. The results of the SMC impedance controller will be shown and discussed in Section 4.2.

3.2   H-Infinity Control

This section will highlight the theory behind H-Infinity control. Standard H-Infinity control background will be explained and lead into H-Infinity control with loop shaping in the form of weighted sensitivities. Also, H-Infinity control theory with plant uncertainties will be elaborated on as well. Much of the information presented in

this section is referenced from Multi-variable Feedback Control: Analysis and Design by Sigurd Skogestad and Ian Postlethwaite unless referenced otherwise [21].

3.2.1 Theory

H-Infinity ($\mathcal{H}_\infty$) control is a frequency-domain optimization and synthesis theory that specifically addresses modeling errors. It is a worst-case-scenario optimal control technique, meaning if little is known about the plant model or the disturbances affecting the system, plan for the worst and optimize. This linear classical optimal robust control method calculates a fixed gain controller that minimizes the norm of the closed loop transfer function, $H(s)$, between the disturbances/reference/model error input(s), w, and the selected performance output(s), z. The H-Infinity norm of a transfer function is the peak value of that transfer function over a frequency range.

$$||H(s)||_\infty = max|\bar{\sigma}(H(j\omega))| \tag{3.13}$$

$\bar{\sigma}$ is the maximum singular value. Optimizing a controller that minimizes those peaks in the closed loop transfer function(s) from ω to z allows for the disturbance/reference/modeling error inputs to have a minimum possible effect on the chosen performance output. This characteristic creates a high margin of robustness toward disturbances and plant uncertainties.

Describing a plant in such a form that is useful for optimization problems involves the use of linear fractional transformations (LFT). A linear fractional transformation is a mapping transfer functions of the form below.

$$F(s) = \frac{a + bs}{c + ds} \tag{3.14}$$

This mapping of transfer functions allows easy access and use of closed loop trans-
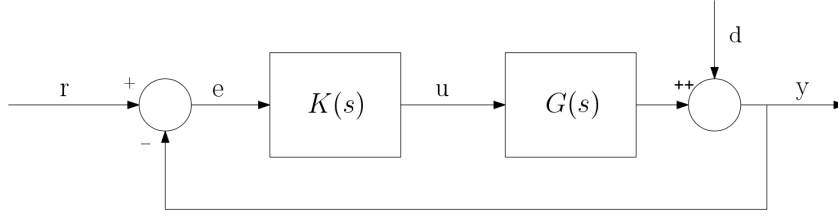
Figure 31: Closed Loop System with Disturbance Input

fer functions for optimal control problems. Any closed loop system can be put into LFT form. Fundamentally, a feedback control system with a disturbance input is a great example to explain the conversion. The comparisons between the closed loop feedback and LFT forms is as simple as matching up variables. Simply, disturbance/reference/modeling error variable, ω, in the LFT consists of the reference variable, r, and the disturbance variable, d, in any order. The performance variable, z, in the case of this feedback system is the error, e. The control input, u, and the measured variable, y, are the same in both forms. An LFT is a standard form for block diagrams when designing and analyzing a robust controller.
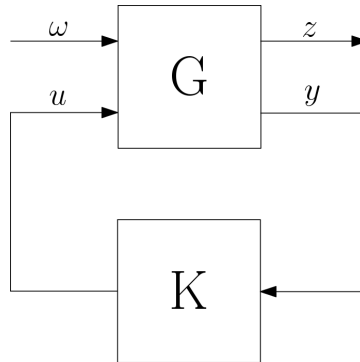
Figure 32: LFT Block Diagram Standard Form

The state space representation of a feedback control system with disturbance inputs can be shown in a two port state space representation.

$$
\begin{bmatrix} \dot{x} \\ z \\ y \end{bmatrix} = \begin{bmatrix} A & B_1 & B_2 \\ C_1 & D_{11} & D_{12} \\ C_2 & D_{21} & D_{22} \end{bmatrix} \begin{bmatrix} x \\ w \\ u \end{bmatrix} \tag{3.15}
$$

45

To extract the state space representation of a LFT block diagram structure shown in Figure 32, the output equations z and y can be extracted from the two port state space and described in its own state space.

$$\begin{bmatrix} z \\ y \end{bmatrix} = \begin{bmatrix} D_{11} & D_{12} \\ D_{21} & D_{22} \end{bmatrix} \tag{3.16}$$

$$u = Ky \tag{3.17}$$

LFT form allows for the straightforward computation of closed loop transfer functions between disturbance/reference/modeling error inputs, w to performance outputs, z, which is advantageous when attempting to minimize the norm of said transfer function(s).

$$T_{zw} = F_l(G, K) = D_{11} + D_{12}K(I - D_{22}K)^{-1}D_{12} \tag{3.18}$$

As stated before, obtaining the optimal H_∞ controller involves finding a controller such that $||T_{zw}||_\infty$ is minimized. In special cases, such as in this thesis, a sub-optimal controller is more practical for implementation. In that case, given $\gamma > 0$, a sub-optimal controller can be found such that $||T_{zw}||_\infty < \gamma$, where γ is a lower bound on the optimization of the closed loop transfer function(s); meaning that the optimization will stop and produce a controller at a specified $||T_{zw}||_\infty$ instead of the smallest $||T_{zw}||_\infty$ it can find. Initial assumptions that must hold when designing an $\mathcal{H}_\infty$ controller, in continuous time using the Riccati method, are the following:

1. (A, B_1) must be controllable.

2. (A, C_2) must be observable.

3. $\begin{bmatrix} A - j\omega & B_2 \\ C_1 & D_{12} \end{bmatrix}$ must have full column rank for all ω.

46

4. $\begin{bmatrix} A - j\omega & B_1 \\ C_2 & D_{21} \end{bmatrix}$ must have full row rank for all ω.

The Riccati algorithm is extremely mathematically intensive and cumbersome to explain. The work of Doyle et al., the group of researchers who created and verified the $\mathcal{H}_\infty$ and $\mathcal{H}_2$ controller synthesis mathematics, explains precisely the mathematical theory behind the algorithm [3]. Also, A. Megretski elaborates on the algorithms for $\mathcal{H}_\infty$ optimization of the Ricatti-based approach [12]. The goal of this thesis is not to educate the reader on the detailed theory, but to provide an overview of the theory that is useful for application.

The Robust Control Toolbox in Matlab has many functions that either perform $\mathcal{H}_\infty$ synthesis directly or a variation such as $\mathcal{H}_2$ synthesis or $\mathcal{H}_2/\mathcal{H}_\infty$, multi-model/multi-objective synthesis with pole placement. Those functions are `hinfsyn`, `h2syn`, and `msfsyn`, respectively. This thesis will describe a method for using `hinfsyn`. `hinfsyn` has the ability to preform $\mathcal{H}_\infty$ synthesis using multiple methods such as the Riccati-based algorithm, the Linear Matrix Inequality-based algorithm, and the Maximum Entropy algorithm. Used in this thesis is the Ricatti-based algorithm. Below is a general description of the MATLAB function `hinfsyn`,

$$[\text{K,CL,GAM,INFO}] = \text{hinfsyn(P,NMEAS,NCON,KEY1,VALUE1,KEY2,VALUE2,...)} \qquad (3.19)$$

where `P` is the plant represented in (3.15) and (3.16). `NMEAS` is the number of measured variables, y, from the plant used by the controller, `NCON` is the number of control variables, u, from the controller to the plant. The `KEY` and `VALUE` placeholders represent alterations to the controller synthesis algorithm.

```
   KEY       |VALUE   | MEANING
  ------------------------------------------------------------------
  'GMAX'    | real   | initial upper bound on GAM (Inf default)
  'GMIN'    | real   | initial lower bound on GAM (0 default)
  'TOLGAM'  | real   | relative error tolerance for GAM (.01 default)
  'METHOD'  |        | H-infinity solution method:
            |'ric'   | - (default) standard 2-Riccati solution, DGKF1989
            |'lmi'   | - LMI solution, Packard 1992, Gahinet 1994
            |'maxe'  | - maximum entropy, HINFSYNE, Glover-Doyle 1988
  'S0'      | real   |   (default=Inf) frequency S0 at which entropy is
            |        |       evaluated, only applies to METHOD 'maxe'
  'DISPLAY' |'on/off'| display synthesis information to screen,
            |        |   (default = 'off')
  ------------------------------------------------------------------
```

Figure 33: `hinfsyn` Algorithm Modification Chart

`K` is the synthesized $\mathcal{H}_\infty$ controller, `CL` is the closed loop system, `GAM` is the $\mathcal{H}_\infty$ cost variable, γ, and `INFO` is additional information relating to the method used.

3.2.1.1 Mixed Sensitivity Weighting

Weights hold a large significance in many robust control theories commonly used today. A weight on a signal is either a scalar or transfer function that shapes a signal in the frequency domain to a designers specifications. Weights fit into the $\mathcal{H}_\infty$ control design problem by shaping different transfer functions found within a closed loop feedback controller.
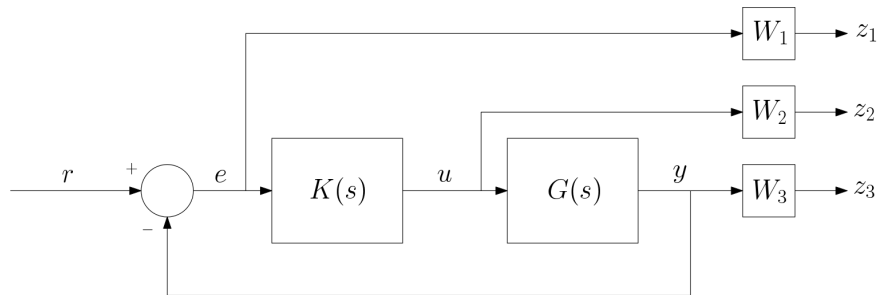
Figure 34: Weighted Plant with Feedback

The typical signals and transfer functions shaped in $\mathcal{H}_\infty$ control weighting are the sensitivity transfer function, S, the control signal, u, and the complementary

48

sensitivity transfer function, T. The sensitivity transfer function, S, of a control system describes the performance of a closed loop system and is the closed loop transfer function from the reference, r, to the error, e.

$$S(s) = \frac{1}{1 + G(s)K(s)} \tag{3.20}$$

A typical weight shape for the sensitivity transfer function is of the form seen below.

$$W_1(s) = \frac{\frac{s}{M} + \omega_c}{s + \omega_c A} \tag{3.21}$$

This weight, $\frac{1}{W_1(s)}$, acts as an upper bound on S, where A is the low frequency gain, M is the high frequency gain, and ω_c is the crossover frequency. This upper bound allows the performance variable magnitude to be shaped in such a way that meets the performance requirements specified by the designer and bounds the performance variable, z, to a frequency range that aids in the synthesis of a practical controller.

The control weight, W_2, is typically a scalar value, which is effectively a gain on the transfer function from the reference, r, to the control, u.

$$R(s) = \frac{K(s)}{1 + G(s)K(s)} \tag{3.22}$$

The weight is not required to be a scalar, but much of the literature dealing with weighted feedback systems specify a scalar value as it aids in the synthesis of a practical controller. Alternative control weight types may be pass-band filters that limit the control authority to a frequency range needed based on the application.

The final weight, W_3, is a weight on the complementary sensitivity, T, which is the transfer function from the reference, r, to the output, y.

$$T(s) = \frac{G(S)K(s)}{1 + G(s)K(s)} = I - S \tag{3.23}$$

49

The complementary sensitivity transfer function is a measure of the disturbance rejection properties of the feedback system. Most closed loop systems prefer to eliminate high frequency disturbances that negatively impact the overall performance of the system. In order to accomplish this goal in the $\mathcal{H}_\infty$ controller synthesis, the weight shape presented below is a common solution.

$$W_3(s) = \frac{s + \frac{\omega_c}{M}}{As + \omega_c} \tag{3.24}$$

This weight, $\frac{1}{W_3(s)}$, acts as an upper bound on T, where A is the low frequency gain, M is the high frequency gain, and ω_c is the crossover frequency. This upper bound allows the complementary sensitivity magnitude to be shaped in such a way that meets the disturbance rejection requirements specified by the designer. The weights previously presented are common to feedback controllers. The shape of the weights is entirely up to the designer and relative to the problem at hand.

Once the weights have been created, they can be factored into the $\mathcal{H}_\infty$ controller design process by using a stacking approach. The stacking approach groups the weighted transfer functions by stacking them vertically inside a vector, N.

$$N = \begin{bmatrix} W_1 S(s) \\ W_2 R(s) \\ W_3 T(s) \end{bmatrix} \tag{3.25}$$

The maximum singular value of this matrix can be calculated for all frequencies,

$$||N||_\infty = max|\bar{\sigma}(N(j\omega))| \tag{3.26}$$

where $\bar{\sigma}(N)$ is the Euclidean norm of a vector.

$$\bar{\sigma}(N) = \sqrt{|W_1 S(s)|^2 + |W_2 R(s)|^2 + |W_3 T(s)|^2} \tag{3.27}$$

Now, the $\mathcal{H}_\infty$ controller synthesis objective is to find a controller that minimizes the maximum singular value of matrix N over all frequencies.

When using weights in `hinfsyn`, those weights must be combined with the plant state space to create an augmented plant state space. That augmented plant state space is then used as the variable P in the `hinfsyn` function. MATLAB has alternative functions such as `augw`, which creates an augmented negative feedback plant with specified weights. Another helpful function with synthesizing a controller for a negative feedback plant is the `mixsyn` function. The ordinary plant as well as the weights can be specified in the function. It then creates and augmented state space and synthesizes a controller in a single step.

3.2.2   Example

The plant (1.2) and impedance relation (1.3) of the elementary examples shown at the beginning of Chapter 1 and Section 3.1.2 will be used to show a basic $\mathcal{H}_\infty$ impedance controller synthesis. The plant and impedance relation must be converted to the LFT state space representation shown in (3.15) and (3.16). State and input variables are specified below.

$$x_1 = x, \quad x_2 = \dot{x}, \quad x_3 = x_I, \quad x_4 = \dot{x}_I \tag{3.28}$$

$$u_1 = F_P, \quad u_2 = F_A \tag{3.29}$$

Using the specified state and input variables, state equations can be constructed from (1.2) and (1.3)

$$\dot{x}_1 = x_2$$
$$\dot{x}_2 = \tfrac{1}{m}u_2 - \tfrac{1}{m}u_1$$
$$\dot{x}_3 = x_4 \quad (3.30)$$
$$\dot{x}_4 = \tfrac{1}{M}u_1 - \tfrac{K}{M}x_3 - \tfrac{B}{M}x_4$$

These state equations are represented in state space form below according to the specifications outlined by the MATLAB function `hinfsyn`. Control inputs to the plant and measured plant outputs to the controller must be last in the respective vectors of inputs and outputs.

$$
\begin{bmatrix} \dot{x}_1 \\ \dot{x}_2 \\ \dot{x}_3 \\ \dot{x}_4 \end{bmatrix}
=
\begin{bmatrix}
0 & 1 & 0 & 0 \\
0 & 0 & 0 & 0 \\
0 & 0 & 0 & 1 \\
0 & 0 & -\tfrac{K}{M} & -\tfrac{B}{M}
\end{bmatrix}
\begin{bmatrix} x_1 \\ x_2 \\ x_3 \\ x_4 \end{bmatrix}
+
\begin{bmatrix}
0 & 0 \\
-\tfrac{1}{m} & \tfrac{1}{m} \\
0 & 0 \\
-\tfrac{1}{M} & 0
\end{bmatrix}
\begin{bmatrix} u_1 \\ u_2 \end{bmatrix}
\quad (3.31)
$$

$$
\begin{bmatrix} z \\ y_1 \\ y_2 \\ y_3 \\ y_4 \\ y_5 \end{bmatrix}
=
\begin{bmatrix}
-1 & 0 & 1 & 0 \\
1 & 0 & -1 & 0 \\
1 & 0 & 0 & 0 \\
0 & 1 & 0 & 0 \\
0 & 0 & 1 & 0 \\
0 & 0 & 0 & 0
\end{bmatrix}
\begin{bmatrix} x_1 \\ x_2 \\ x_3 \\ x_4 \end{bmatrix}
+
\begin{bmatrix}
0 & 0 \\
0 & 0 \\
0 & 0 \\
0 & 0 \\
0 & 0 \\
1 & 0
\end{bmatrix}
\begin{bmatrix} u_1 \\ u_2 \end{bmatrix}
\quad (3.32)
$$

The performance variable, z, is the difference between the actual position of the mass and the target impedance position. This performance specification is critical to the formulation of a robust impedance controller. A block diagram representing the

performance specification can be seen below.
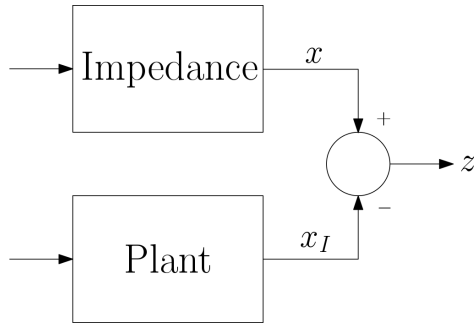
Figure 35: $\mathcal{H}_\infty$ Performance Variable Block Diagram Representation

Using (3.19) with NMEAS = 5 and NCON = 1 will produce an optimal controller that produces an actuator force that allows the mass to act as a mass-spring-damper when acted upon by the force of the person. Adjusting GMIN to different values produces a sub-optimal controller with decreased performance and robustness but may be more practical in application.

Notice that weights are not used in this elementary example of $\mathcal{H}_\infty$ impedance control. This was done for simplicity in showing the setup of an $\mathcal{H}_\infty$ impedance control problem unconstrained by weights. Weights will most likely provide performance and disturbance rejecprtion benefits when applied to this example problem, but that is not the goal of this problem. Also, the number of measured plant outputs to the controller is a design choice made by the engineer. The number of measured outputs given to the controller effects all aspects of the closed loop performance and disturbance rejection capabilities and must be chosen accordingly.

3.2.3   Controller Design

The $\mathcal{H}_\infty$ impedance controller design will be broken down into 3 different categories. These categories are based on the multiple attempts to produce a practical controller with adequate performance and disturbance rejection capabilities. Each

category elaborates on the $\mathcal{H}_\infty$ control design theory pertaining to proper weighing and plant modeling uncertainty implementation. The first attempt to produce an $\mathcal{H}_\infty$ impedance controller uses only a nominal plant with constraining weights on the performance, control, and measured variables. Weights on disturbance inputs may be present to further constrain the plant during design. The second attempt includes weights as well as a structured parametric representation of the uncertainties present in the plant. The theory of structured parametric plant uncertainty modeling can be understood by reading Section 2.2.2.1. The final attempt includes weights and a representation of the un-modeled dynamics of the plant. The un-modeled dynamics are taken into consideration using a multiplicative model uncertainty description. This type of uncertainty description can be understood by reading Section 2.2.2.3. The controller design processes for all three attempts will be shown and the results will be discussed in the next chapter.

3.2.3.1 Weighted Plant

In order to create a weighted plant for the $H\infty$ controller synthesis, an augmented plant consisting of the CSU 4OptimX plant, the target impedance, and the weights for the performance, control, and disturbance signals must be created. Creating a state space for this application involves specifying the states of the augmented plant to be the motor position and velocity of the CSU 4OptimX as well as

the position and velocity of the target impedance.

$$
\begin{aligned}
x_1 &= \theta_m & U_1 &= F & y_1 &= x_1 - v_1 \\
x_2 &= \dot{\theta}_m & U_2 &= \theta_I^d & y_2 &= \theta_m \\
v_1 &= \theta_I & U_3 &= \dot{\theta}_I^d & y_3 &= \dot{\theta}_m \\
v_2 &= \dot{\theta}_I & U_4 &= \ddot{\theta}_I^d & y_4 &= \theta_I \\
& & U_5 &= U & y_5 &= \dot{\theta}_I \\
& & & & y_6 &= \theta_I^d \\
& & & & y_7 &= \dot{\theta}_I^d \\
& & & & y_8 &= \ddot{\theta}_I^d \\
& & & & y_9 &= F
\end{aligned}
\tag{3.33}
$$

The input variables are the impedance force, desired target impedance position, velocity, and acceleration trajectories, and the control voltage. The outputs have all been described and can be inferred from past variable explanations. Notice that reference inputs U_1 through U_4 are also outputs in the state space. This is done so that the `hinfsyn` function in MATLAB knows the number of outputs to the controller. Normally, reference variables would be routed to the controller outside of the state space. State derivative equations were calculated from differential equations (2.3) and (3.8).

$$
\begin{aligned}
\dot{x}_1 &= x_2 \\
\dot{x}_2 &= \frac{K_T}{J_T}U_5 - \frac{nd}{J_T}U_1 - \frac{b_T}{J_T}x_2 \\
\dot{v}_1 &= v_2 \\
\dot{v}_2 &= U_4 - \frac{B}{I}v_2 + \frac{B}{I}U_3 - \frac{K}{I}v_1 + \frac{K}{I}U_2 - \frac{nd}{I}U_1
\end{aligned}
\tag{3.34}
$$

Part of the augmented plant has been constructed. The weights are the next and final addition. The weights chosen for this application are low pass filters for W_1

and W_3 and a scalar value for W_2.

$$W_1(s) = \frac{\frac{s}{M_1} + w_{c1}}{s + A_1 w_{c1}} \quad W_2 = 1 \quad W_3 = \frac{\frac{s}{M_3} + w_{c3}}{s + A_3 w_{c3}} \tag{3.35}$$

The values of the variables for the weights are the following: $M_1 = 2$, $A_1 = 0.0001$, $w_{c1} = 12\frac{rad}{s}$, $M_3 = 2$, $A_3 = 0.0001$, and $w_{c3} = 12\frac{rad}{s}$. The weights were found through a combination of prior knowledge of $\mathcal{H}_\infty$ feedback weights, the signal frequency response shape, and iterative syntheses using different weight shapes. The determination of weights is neither intuitive nor easy for this application. The goal of this thesis is not to propose general weight shapes for $\mathcal{H}_\infty$ impedance applications, but to find weights that produce a well-performing, practical controller. The crossover frequencies, w_c, for the weights were found through Fast Fourier Transform analyses of the associated signals. All dominant frequencies were amplified while non-dominant or negligible frequencies were attenuated. The augmented plant can now be interconnected using the *sysic* function in MATLAB. The block diagram of the augmented plant before weight interconnection is the following figure.
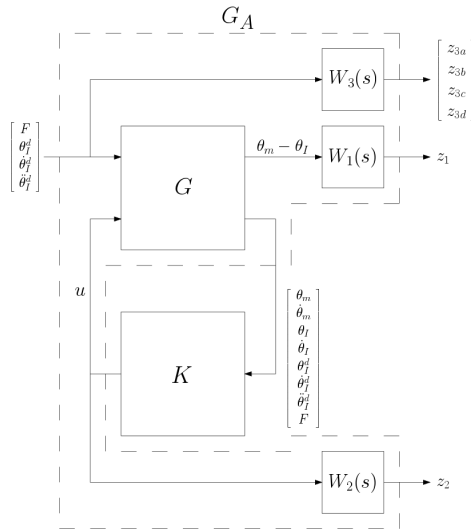

Figure 36: $\mathcal{H}_\infty$ Weighted Closed Loop Plant

G is the state space description of the equations (3.33) and (3.34). G_A is

the augmented plant for the $\mathcal{H}_\infty$ controller synthesis algorithm. All z values are the performance variables. There closed loop transfer functions from inputs U_1 through U_4 will be minimized. Using the `hinfsyn` function in MATLAB with the following setup, an $\mathcal{H}_\infty$ controller for a nominal, weighted CSU 4OptimX plant can be synthesized.

3.2.3.2 Weighted Plant with Structured Parametric Uncertainty

In this section, a controller will be designed that factors in a range of known, possible values of the plant parameters. In order to include this range of plant parameters into the controller synthesis, a technique which is discussed in Section 2.2.2.1 will be used. That technique is called Structured Parametric Uncertainty. Using equations (3.33), (3.33), and (3.35) with identical equation variable values as in the previous sections, an augmented state space can be assembled for $\mathcal{H}_\infty$ controller synthesis.
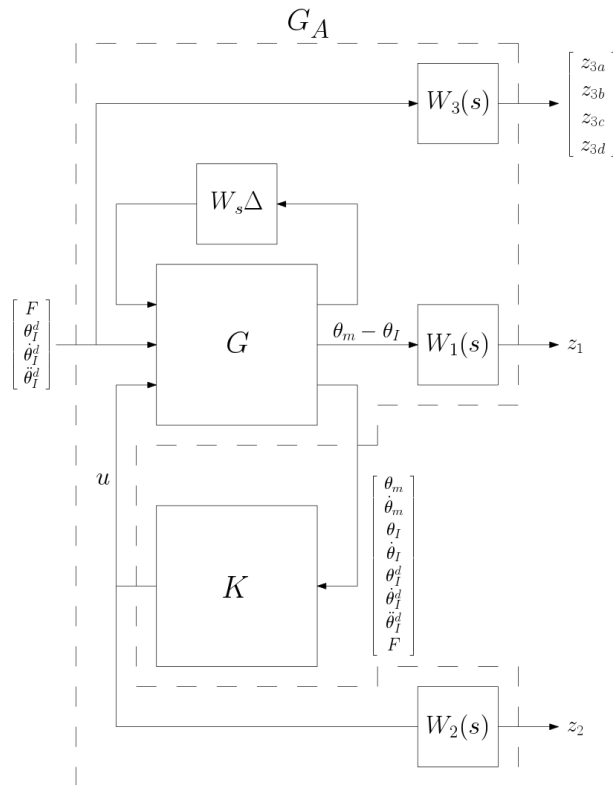

Figure 37: $\mathcal{H}_\infty$ Weighted Closed Loop Plant with Structured Parametric Uncertainty

W_3 is normally a weight shape or matrix of weight shapes. For this thesis the weight will be the following matrix:

$$W_3 = \begin{bmatrix} \bar{K}_T & 0 & 0 \\ 0 & \bar{b}_T & 0 \\ 0 & 0 & \bar{J}_T \end{bmatrix} \tag{3.36}$$

The scalar values have the following values: $\bar{K}_T = 0$, $\bar{b}_T = 3.03$, and $\bar{J}_T = -0.65$. $\bar{J}_T$ is negative in order to represent the direction of the parametric uncertainty between the nominal and true J_T value. The scalar values are multiplied by U, $\dot{\theta}_m$, and $\ddot{\theta}_m$ as well as the 3x3 uncertainty matrix, Δ. Then, the signals are routed back into the plant to complete the loop. For enhanced clarity, the dynamic equation of the CSU 4OptimX plant with structured parametric uncertainty is shown below.

$$J_T\ddot{\theta}_m + \bar{J}_T\Delta\ddot{\theta}_m + b_T\dot{\theta}_m + \bar{b}_T\Delta\dot{\theta}_m = K_T U + \bar{K}_T\Delta U - ndF \tag{3.37}$$

Using G_A as the augmented plant, the structured uncertainty can be taken into consideration during the controller synthesis.

3.2.3.3 Weighted Plant with Multiplicative Uncertainty

In this section, the modeled plant uncertainty is expressed as a multiplicative model uncertainty. One can learn about multiplicative uncertainty as well as $\mathcal{H}_\infty$ controller design in Sections 2.2.2.3 and 3.2.1. The $\mathcal{H}_\infty$ controller design synthesis involves specifying an augmented plant consisting of weights and the modeled multiplicative plant uncertainty. The augmented model can be best represented by viewing Figure 36 in Section 3.2.3.1. Inside plant G, is where the multiplicative uncertainty is modeled. A block diagram representing a properly modeled plant with multiplicative uncertainty is found in Figure 26.

Important to the successful modeling of the multiplicative model error is choosing a weight that represents the error between the true plant and the modeled plant. Using methods found in Section 2.2.2.3, a multiplicative model error weight satisfying that criterion is developed. This weight can be found in Section 2.2.2. The weight, combined with a block representing uncertain dynamics in MATLAB, applies to all plant outputs since all plant outputs suffer from the modeling error as well as anomalies in the control input signal. With this augmented plant representation, an $\mathcal{H}_\infty$ controller is synthesized.

CHAPTER IV

Results and Discussion

The results of this thesis are broken down into three main sections: nominal and uncertain plant results, sliding mode controller results, and $\mathcal{H}_\infty$ controller results. Plant parameter results for the nominal plants of all four motors and uncertain values of motor 2 will be discussed first. Those results are used in the sliding mode and $\mathcal{H}_\infty$ controller designs previously described and factor into the their overall performance. The tracking performance as well as a discussion on implementation feasibility will be elaborated upon. In order to concisely compare the control systems, only results for motor 2 are shown and discussed.

4.1   Plant

The nominal plant parameters were found using methods described in Section 2.2. The results are shown below.

Parameter	Motor			
	1	2	3	4
K_T ($\frac{Nm}{V}$)	0.38	0.59	0.465	0.3275
J_T ($\frac{kg}{m^2}$)	0.0238	0.0326	0.0214	0.0151
b_t (Nms)	0.19	0.2314	0.1305	0.0919

Table V: Nominal Plant Parameters

Using equations (2.8) and (2.7), where the first equation is the numerical transfer function derived from system identification, the parameters can be found by comparing the numerators and denominators of each equation and solving for the variables algebraically. The transfer functions fit the data to an $80 - 85\%$ accuracy. The fit percentage is the Normalized Root Mean Squared Error (NRMSE) between the identified transfer function output and the output data gathered through experimentation. Notice that, even though motors 1 and 4 are identical, they have drastically different plant parameters. This is due to the inability to obtain increased accuracy between the data and the transfer function when performing system identification. Difficulties in obtaining higher accuracy percentages include un-modeled dynamics known to be present in the system such as a torsional stiffness present in the timing belt. The torsional stiffness dynamics were left un-modeled in order to keep the plant model from becoming overly complicated. Additionally, the robust control techniques inherently compensate for such situations. It is a goal of this research to use robust control techniques to compensate for un-modeled dynamics such as the torsional stiffness present in the timing belt. It is not considered to be a problem if that characteristic was the only source of error in the identification. Also, an electrical anomaly present while the data acquisition system is in the loop with the robot causes the control voltage to dip periodically if more than one motor is on at the same time. This anomaly likely skewed the input, output data used for the parameter identification causing the accuracy in fit to be less.

It was also necessary to quantify the amount of uncertainty present in the plant. Due to time constraints, the plant uncertainty was only able to be quantified for motor 2. This was done by identifying the system many more times and comparing the Bode plots of those systems to the nominal system. The plants found by system identification are shown in the following figure. The red line is the nominal plant used and the blue lines represent the uncertain plants.
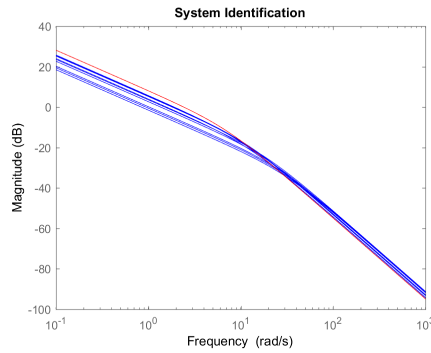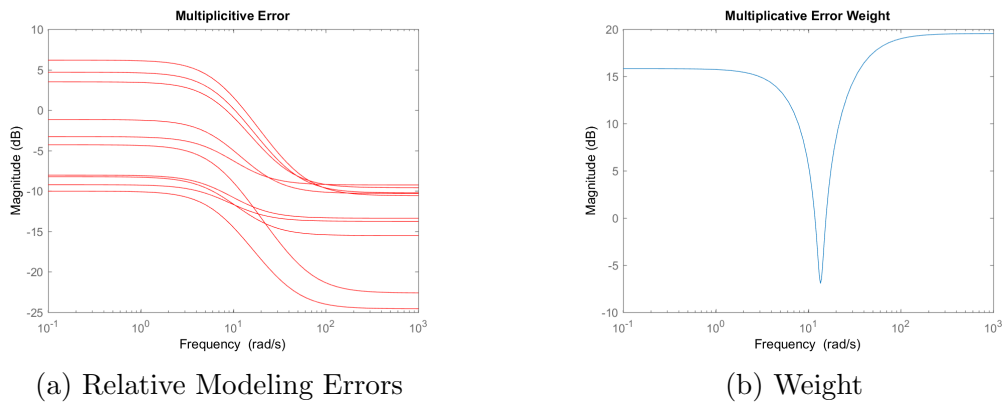

Figure 38: System Identification Plant Uncertainty

These plants are used to construct the multiplicative modeling error weight used in the $\mathcal{H}_\infty$ controller design. The Bode plot of the multiplicative model errors and the associated weight used in Section 3.2.3.3 is shown below.

(a) Relative Modeling Errors   (b) Weight

Figure 39: Multiplicative Uncertainty Errors and Weight

The multiplicative modeling error weight was then found based on equation (2.17). The weight is a 5th order transfer function. As is evident, the relative modeling

errors vary significantly between one another, visually indicating the amount of error between the specified nominal plant and subsequent system identifications of the same plant. As will be shown in future sections, the robust controllers are able to overcome these uncertainties.

4.2   Sliding Mode Control

Sliding mode control was found to be very successful in both simulation and implementation. For that reason, only implementation results will bw shown. Results for the determination of sliding mode control performance comes in three forms. First, the sliding function (3.10) must reach the surface ($s = 0$) in finite time and remain on the surface in between the bounds $\pm\phi$ for the duration of robot activity. Second, adequate position and velocity tracking must be achieved. Velocity tracking is especially important to validate that the target impedance is being produced by the robot during human/machine interaction.

Using a 3 second period sinusoidal position input and a random force input on the robot via human/machine interaction for the last 10 seconds of the test, the following impedance parameters were tested on the robot.

Test	Inertia	Damping	Spring Constant
1	Nominal	Nominal	7
2	Nominal	1	1
3	0.12	Nominal	1
4	0.06	0.6	3.5

Table VI: Impedance Settings for Sliding Mode Controller Verification

All nominal values can be interpreted as the nominal rotational inertia and rotational damping parameters of the plant. It is important to note that the same sliding mode controller gains and sliding function tolerances were used for each test. Results vary when changing these gains.
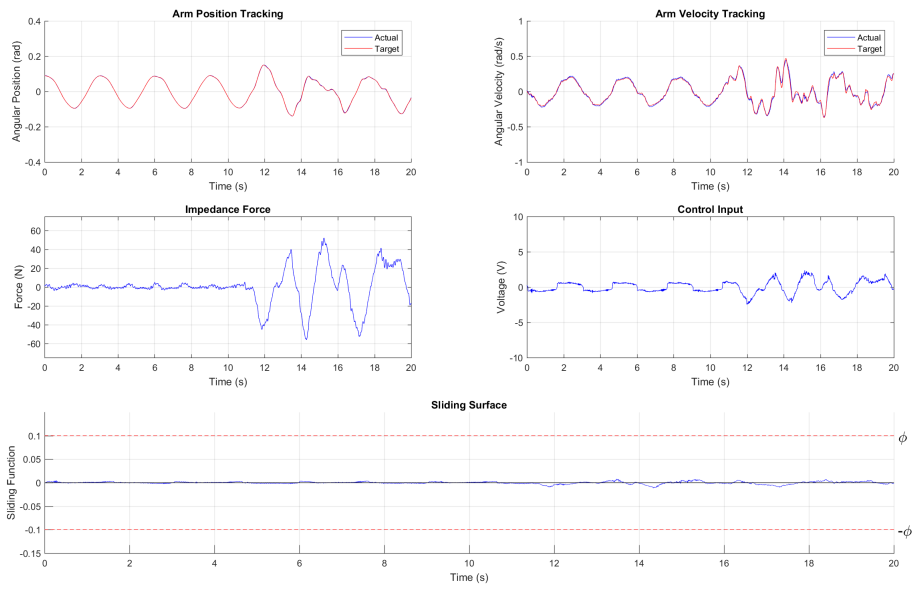
Figure 40: SMC Impedance Verification Test 1 - Motor 2

Figure 41: SMC Impedance Verification Test 2 - Motor 2
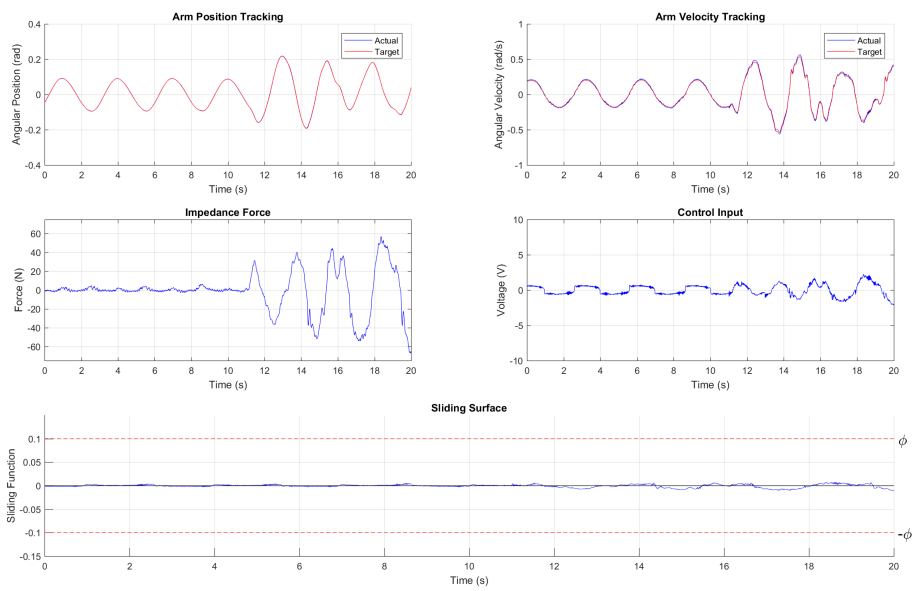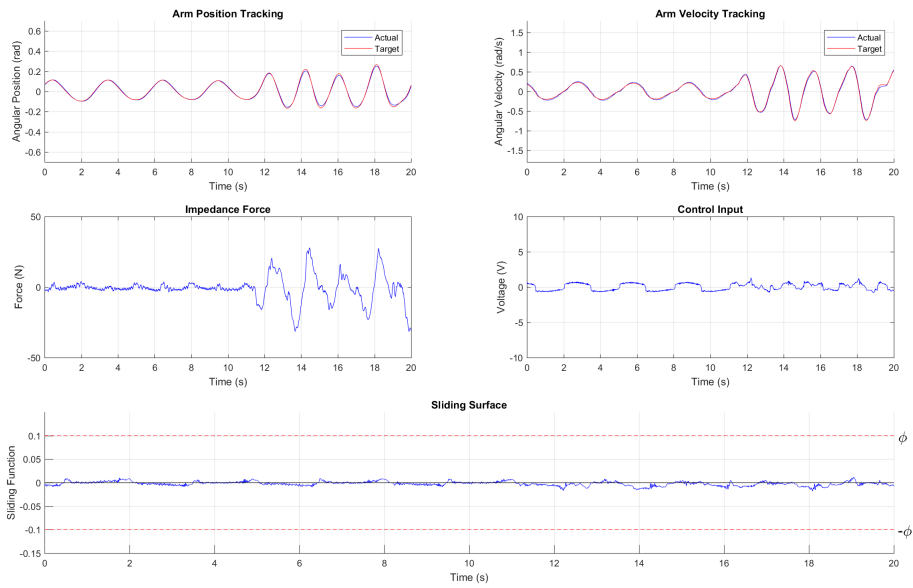
64

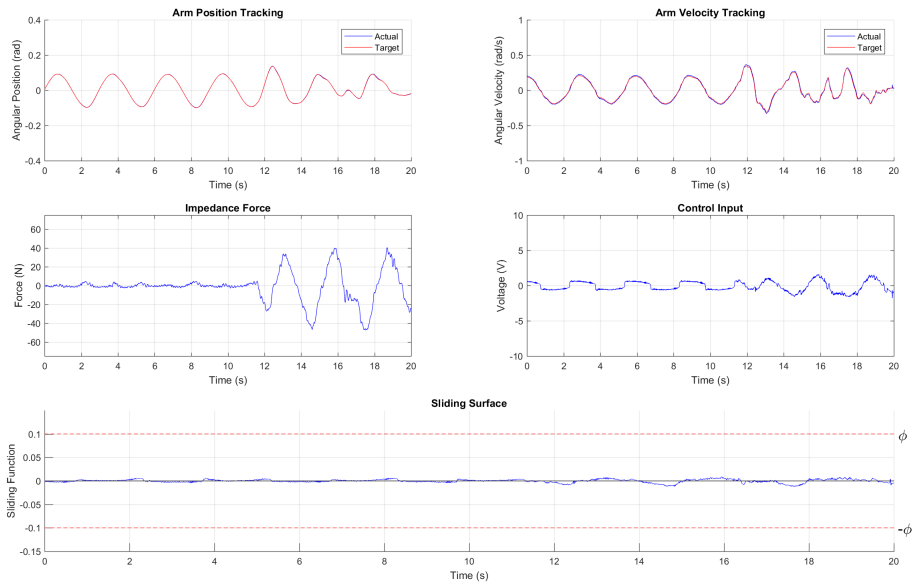Figure 42: SMC Impedance Verification Test 3 - Motor 2

Figure 43: SMC Impedance Verification Test 4 - Motor 2

In all four figures above, the sliding function stayed within the bounds of the sliding surface. Both the arm position and velocity curve tracked the target impedance curve closely. These characteristics ensure that the required target impedance is being met

to an acceptable degree of error. Shown in Table VII is a quantification of the tracking error and chatter for motor 2.

Test	RMS Position Error (%)	RMS Velocity Error (%)	Chatter
1	1.128	5.667	16.06
2	0.516	3.165	18.407
3	4.684	3.648	24.864
4	0.867	3.845	17.166

Table VII: Sliding Mode Control Verification Test Results

The tracking errors were found by applying a root-mean-squared (RMS) average between the actual and target positions and velocities. Motor chatter is a phenomenon that occurs in the control input of electric motor control systems. It is produced by the high frequency switching of the control input signal. When the sliding model tolerance, ϕ, is too small or the gain, η of the controller is too high, the sliding function crosses the sliding surface, $s = 0$, too rapidly for the motor to physically respond. These effects can be detrimental to the lifespan of a motor and must be minimized. The amount of motor chatter present in the control signal is found by performing an fast fourier transform (FFT) analysis on the control signal. All frequencies above a minimum frequency are considered motor chatter in the signal and are summed to produce the final chatter value in the control signal.

$$\text{chatter} = \sum_{i=1}^{n} A_i \text{ where } \omega_1 \geq \omega_{min} \tag{4.1}$$

A_i is the amplitude of each frequency in the FFT plot, ω_{min} is the smallest frequency that does not encompass the dominant or fundamental frequencies of the signal, and n is the number of frequencies plotted in the FFT plot. ω_{min} chosen for this analysis is 2.5 $\frac{rad}{s}$. The main use of this data is to compare its values with the values found upon testing of the $\mathcal{H}_\infty$ controllers later on in the chapter.

Sliding mode is especially valuable due to its non-discriminatory robustness.

The switching action is able to deal with large, un-modeled uncertainties as well as non-linearities of any nature that are present in a system. Sliding mode control is inherently a more robust controller, but, due to time constraints, its level of robustness could not be quantified. A glimpse of its robustness can be seen in its accurate tracking performance in the face of the disturbance anomalies present in the system.

4.3   H-Infinity Control

In this section, the resulting $\mathcal{H}_\infty$ controllers are analyzed for performance and robustness. The designation of weights for the $\mathcal{H}_\infty$ controller synthesis directly determines the performance, disturbance rejection abilities, and implementable practicality of the synthesized controller. It is a delicate balance between those three characteristics. For feedback systems, the weight shapes can be more readily specified due to 3 decades of $\mathcal{H}_\infty$ control application experience. This information is available in most $\mathcal{H}_\infty$ literature. For other systems, such as systems with impedance control, the weights are not directly known and may not be as intuitive. Achieving desired performance and disturbance rejection goals may be possible, but synthesizing a practical controller with small negative closed loop poles poses a challenge to any engineer attempting to implement the $\mathcal{H}_\infty$ control law with impedance control. Small negative closed loop poles consist of far left-hand-plane poles that exceed the Nyquist frequency of the robot. If a closed loop pole exceeds the Nyquist frequency, the system cannot respond to such dynamics since they are faster than the system can reliably observe.

4.3.1   Weighted Plant

The augmented plant consisting of the CSU 4OptimX plant, the target impedance and the associated weighted described in Section 3.2.3.1 synthesized a

controller with satisfactory results in simulation. Below are the plots of the response to an uncertain plant given step inputs for the impedance force and desired position. The impedance parameter values are low for simulation testing. Those parameters are 1 for K and the nominal values of the plant damping and inertia for both B and I. Low impedance parameters were used in order to test the feasibility of the controller. Assessing performance using larger impedance parameters will occur if the controller is feasible for implementation.
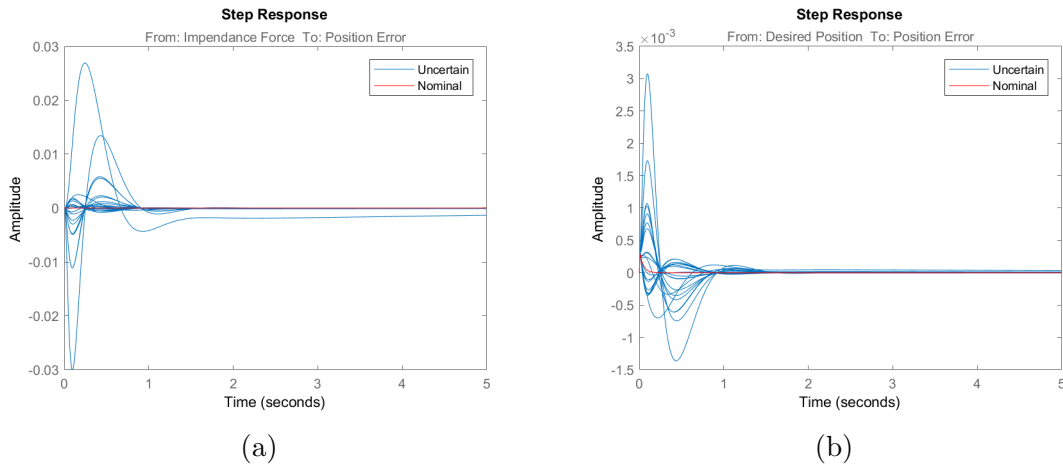

Figure 44: Simulated Weighted $\mathcal{H}_\infty$ Closed Loop Step Response

Figure 44a represents the step response from an impedance force input to the position error. The magnitude of the impedance force step response is 100 N, which is the max force seen during testing of the sliding mode controller. Figure 44b represents the step response from a desired potion input to the position error. The magnitude of the desired motor position step response is 3 radians, which corresponds to 44.55° of arm rotation due to the compounding of gear ratios between the motor shaft and the arm. Although the overshoot and final values of the uncertain responses become worse, they converge. It is also worthwhile to note that the magnitude of the overshoot in Figure 44a is worse than the overshoot of Figure 44b. This fact is also evident in the Bode plot of the same inputs and outputs. Large amounts of error between the nominal and uncertain plants occur in the frequency range of operation from 10^{-1} to
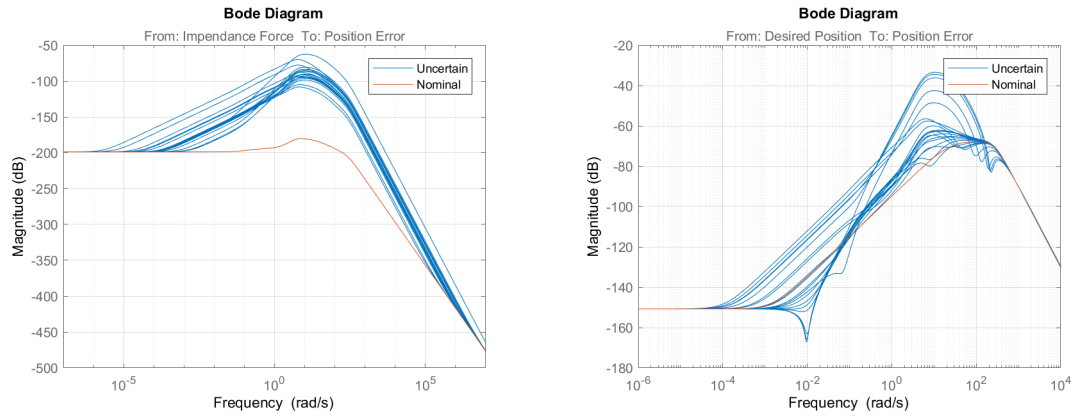
$10^2 \; \frac{rad}{s}$.

Figure 45: Simulated Weighted $\mathcal{H}_\infty$ Closed Loop Frequency Response

Off-nominal plant parameters in the closed loop system produce larger error in the frequency response when compared to the nominal closed loop system. Overall, this data shows that input impedance forces have a larger effect on the position error than the desired impedance motor position input.

It is also worthwhile to check the initial condition response of the closed loop system to ensure that it converges to a final value in a timely manner. In this case, the system converges very closely to zero position error in all cases. Zero final value convergence is not a requirement for this design. Instead, it is important that the system converges from an initial position as quickly as possible.
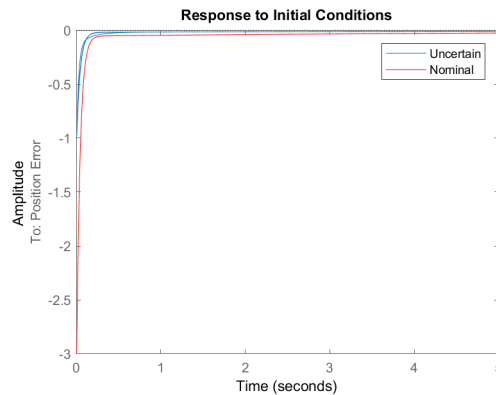

Figure 46: Simulated Weighted $\mathcal{H}_\infty$ Closed Loop Initial Condition Response

The closed loop system converges in under a half second from a worst-case-scenario initial condition. The initial value of the actual arm position was set to be 44.55° away from the target impedance arm position. This displacement represents the maximum displacement likely to be seen between those two states.

Lastly, it is important to look at the closed loop poles to confirm stability. Also, the placement of the poles and zeros tell a great deal about the closed loop system performance.
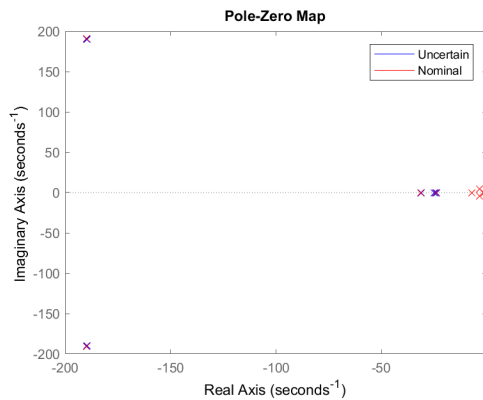

Figure 47: Weighted $\mathcal{H}_\infty$ Closed Loop Pole-Zero Map

The largest negative real part of the closed loop poles, -190 s^{-1} is well under the 500 s^{-1} Nyquist frequency that the closed loop system must adhere to so that the signals of the system do not have a faster frequency than the sampling frequency of the system. If this happens, those signals will become aliased and unreliable.

Although the system is already stable for the uncertain plant, it is important to know the amount of extra uncertainty that causes closed loop instability. To obtain such information, a robust stability analysis is performed on the closed loop system. The analysis shows that the closed loop system is marginally stable for the defined model uncertainty. It can tolerate up to 99.8% of the modeled uncertainty before instability occurs. Normally, this outcome would not be implementable, but the instability occurs at an infinite frequency. The system does not have the ability to respond to frequencies higher than the sampling frequency of 1000 s^{-1}. The system

is marginally stable in theory but can be considered robustly stable for the defined modeled uncertainty. Any uncertainty outside of the defined range will cause the closed loop system to become unstable.

Implementation results using the same tests run on the sliding mode controller are shown below. The test parameters can be found in Table VI. Using a sinusoidal tracking input of $3 \frac{rad}{s}$ and a random impedance force input from 10 seconds to 20 seconds, the same tests are run to quantify the root mean squared (RMS) error in position and velocity as well as the amount of chatter present in the control signal. Motor 2 is used as the testing motor.
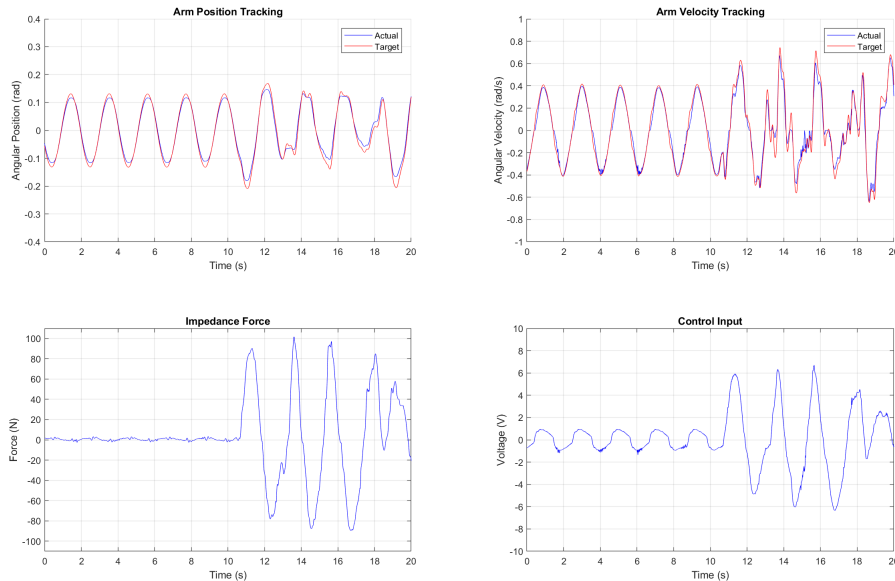

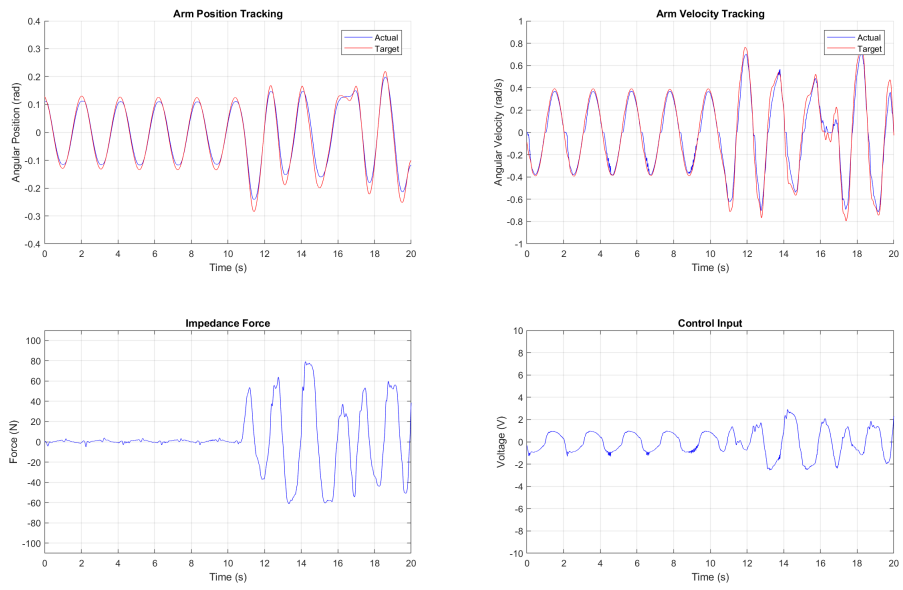
Figure 48: Weighted $\mathcal{H}_\infty$ Verification Test 1
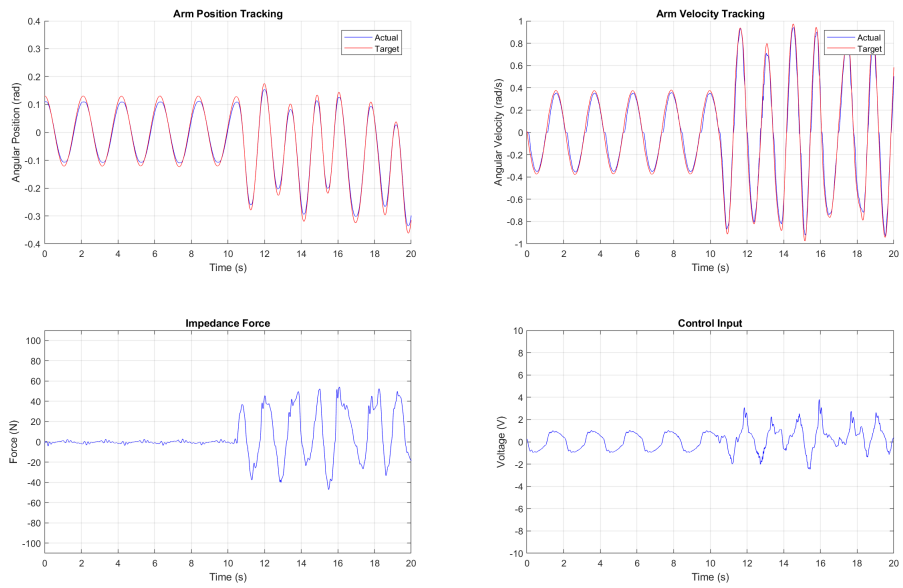
Figure 49: Weighted $\mathcal{H}_\infty$ Verification Test 2

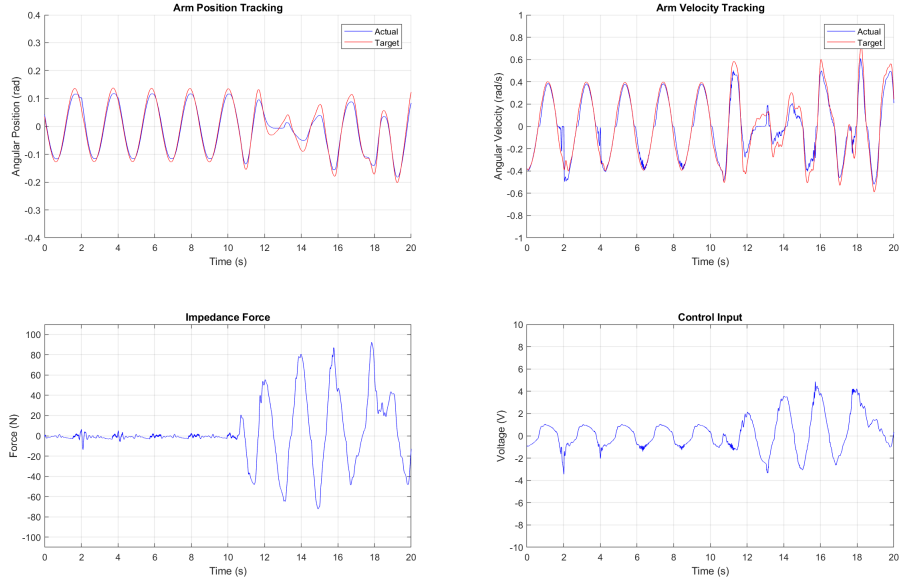Figure 50: Weighted $\mathcal{H}_\infty$ Verification Test 3

Figure 51: Weighted $\mathcal{H}_\infty$ Verification Test 4

Upon visual inspection of the plots, tracking for both position and velocity is fairly accurate. A table showing the RMS errors in the position and velocity is shown below.

Test	RMS Position Error (%)	RMS Velocity Error (%)	Chatter
1	8.527	10.219	11.096
2	11.724	13.264	10.299
3	7.114	6.358	13.087
4	16.758	13.155	16.807

Table VIII: Weighted $\mathcal{H}_\infty$ Verification Test Results

Comparing the results in this table to the results of the sliding mode controller in Table VII, it is immediately apparent that the $\mathcal{H}_\infty$ controller produces larger tracking errors in both position and velocity for each test. The comparison of both tables also shows that the $\mathcal{H}_\infty$ controller produces less chatter in the motor input signal for every test. This is an expected result since the sliding mode controller has inherent switching behavior associated with its operation. Weighing the benefits associated with decreased motor chatter compared to an increase in tracking error is dependent on the predicted operating life of the robot as well as the need for precise

tracking. As a solution to this debacle, the sliding mode controller can be used when precise tracking is needed and the $\mathcal{H}_\infty$ controller can be used to extend the life of the robot.

4.3.1.1   Weighted Plant with Structured Parametric Uncertainty

Using the theory in Section 2.2.2.1 and applying it in Section 3.2.3.2, an $\mathcal{H}_\infty$ controller is synthesized that factored in the structured plant uncertainty. Unfortunately, the resulting controller is not practical for application or even in simulation. Shown below is the step simulation of the closed loop system.
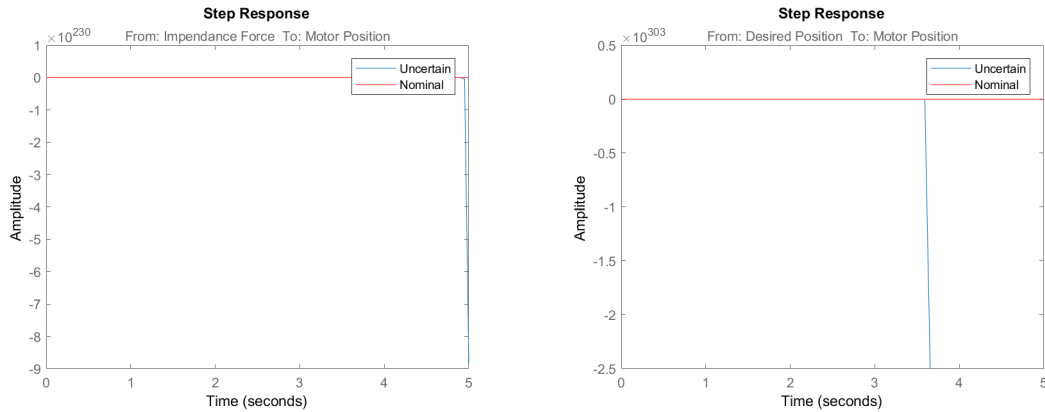

Figure 52: Simulated Weighted $\mathcal{H}_\infty$ with Structured Parametric Uncertainty Closed Loop Step Response

As is evident, the resulting step response is unstable. An examination of the poles of the closed loop system verify the results shown in the step response.
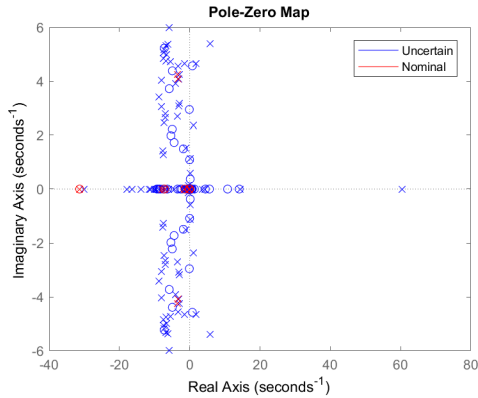
Figure 53: Weighted $\mathcal{H}_\infty$ Closed Loop with Structured Parametric Uncertainty Pole-Zero Map

As a final check to quantify the amount of instability in the uncertain plant, a robust stability analysis is conducted. The results show that the uncertain closed loop system can only tolerate up to 5.91% of the modeled uncertainty. Instability occurs as a frequency of 4.46 $\frac{rad}{s}$, which is a normal operating frequency of the system. This controller does not have the ability to successfully control or stabilize the CSU 4OptimX plant.

4.3.1.2   Weighted Plant with Multiplicative Uncertainty

Using the theory presented in Section 2.2.2.3 along with the weighted plant constructed in Section 3.2.3.1, a plant with multiplicative uncertainty is constructed. Compared to the results of the previous controllers in this section, using a multiplicative uncertainty representation provides initially provides the most promising results. Shown below are the simulated step responses from input impedance force and desired impedance target motor position to the position error between the target impedance motor position and the actual motor position.
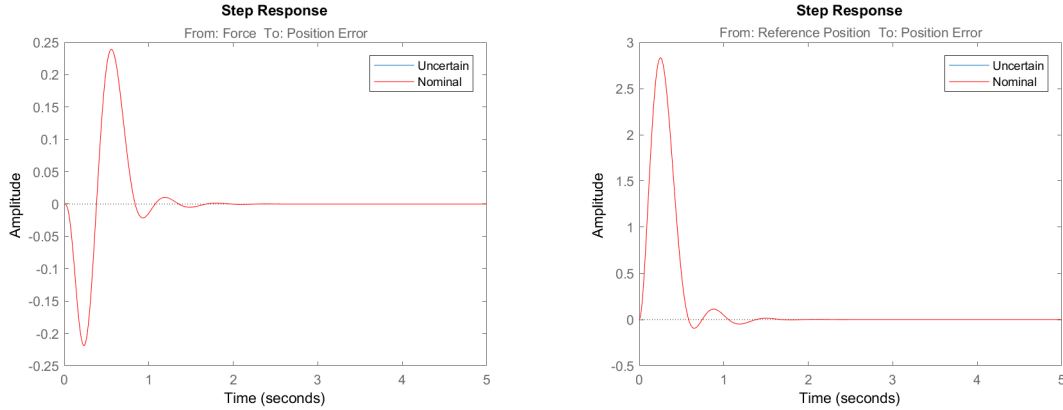
Figure 54: Simulated Weighted $\mathcal{H}_\infty$ with Multiplicative Uncertainty Closed Loop Step Response

It is shown in the graph that the closed loop system response in unaffected by the uncertainty in the plant since there is no variation in the response from nominal. The peak response for each plot from left to right is 0.239 rad and 2.83 rad, respectively. The settling times are 1.51 seconds and 0.987 seconds. For this controller, the reference position step input of 3 rad produces a 1084% larger deviation in the position error, but reaches zero steady state error a half a second faster than the impedance force step response. For this application, it is important that both the settling time and the position error be kept as small as possible. Also, these step responses are considered worst-case-scenario step responses. Less sudden responses with smaller amplitudes are more likely to be seen. Thus, the closed loop system is likely to response with smaller position errors and settling times.

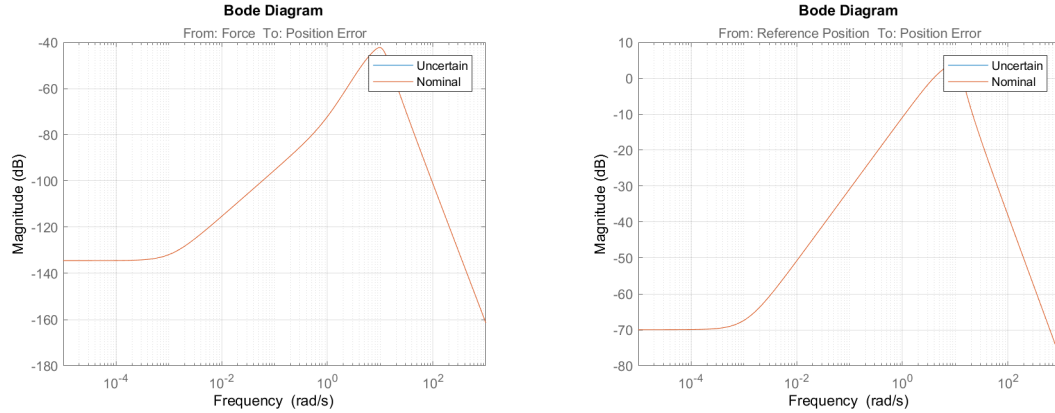The response characteristics above can also be seen in the Bode plots.

Figure 55: Simulated Weighted $\mathcal{H}_\infty$ Closed Loop Frequency Response

Each plot has a peak gain of -42.3 dB at 9.87 $\frac{rad}{s}$ and 4.21 dB at 9.29 $\frac{rad}{s}$ along with similar frequency response shapes. The larger, positive peak gain in the desired impedance position Bode plot can be correlated with a larger peak response in the desired impedance position step response. As assumed from the step response plots, there is no uncertain plant Bode plots that deviate from the nominal plot, meaning that the closed loop system is extremely robust to plant uncertainty.

In order to quantify the amount of robustness to plant uncertainties in the closed loop system, a robust stability analysis is performed. The analysis shows that the closed loop system is robustly stable for all modeled uncertainty. The system can tolerate up to 1,000,000% of the modeled uncertainty. This is an unrealistic result for for any fixed gain controller for this application. Compared to the robust stability results of the previous $\mathcal{H}_\infty$ controllers, this result doesn't make sense. Further analysis will show other problems in the controller that explain this result.

Lastly, a look at the poles of the closed loop system will give insight into the performance and practicality of the controller.
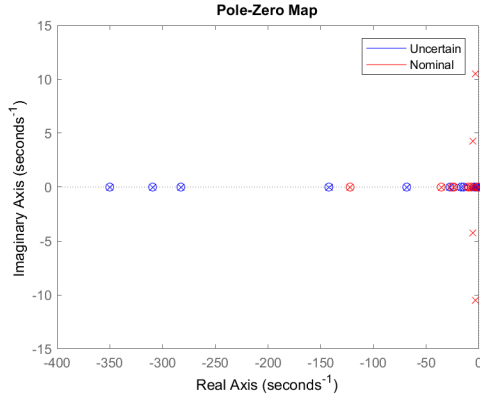
Figure 56: Weighted $\mathcal{H}_\infty$ Closed Loop Pole-Zero Map

The map above shows pole-zero cancellations for all poles and zeros in the uncertain closed loop plant, meaning the uncertain system has no dynamics. A system with no dynamics is the easiest system to control. If this controller cancels the robots dynamics upon implementation, then the closed loop system should show near perfect performance and disturbance attenuation. This result appears unrealistic as well compared to other controllers synthesized for this robot. This conclusion is most likely the reason for the very large robustness tolerance percentage mentioned earlier. The nominal plant, however, has dynamics. Its largest negative pole is at -8.43 $\frac{rad}{s}$.

The results of the controller upon implementation to the CSU 4OptimX are shown below. The impedance parameters used for this test are the parameters of test 1 in Table VI.
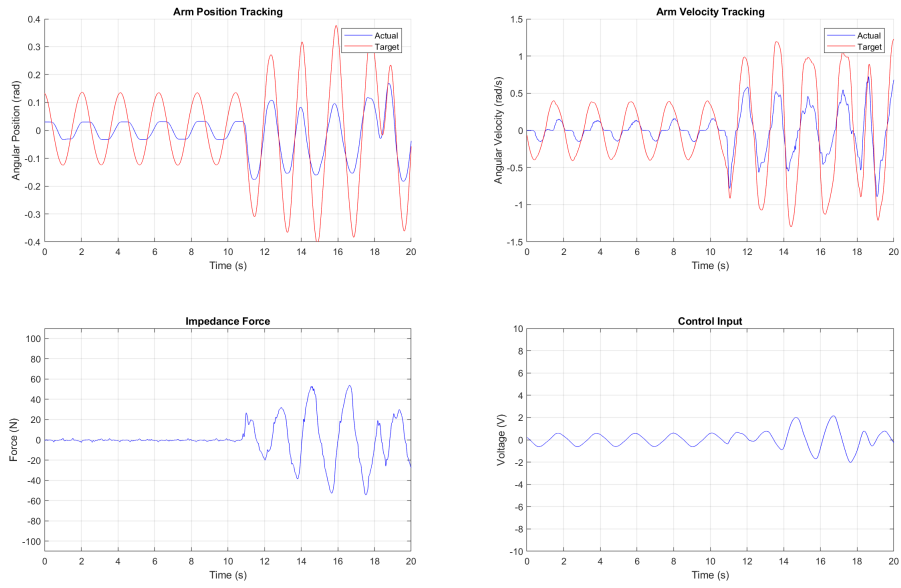
Figure 57: Weighted $\mathcal{H}_\infty$ with Multiplicative Uncertainty Verification Test

The controller shows poor tracking results on the very first test. These results do not warrant further testing and analysis as its performance is not comparable to the other controllers. This controller is unsuccessful at controlling the CSU 4OptimX and will not be used.

CHAPTER V

Conclusions & Recommendations

The main goal of this thesis is to design, analyze, and implement a robust impedance controller as the foundational control for the CSU 4OptimX. The sliding mode control law proves to be an immediate success and is currently the main control on the robot. Its ability to track the desired impedance position, attenuate disturbances, and change impedance parameters instantaneously without having to redesign the controller cannot be matched by the fixed gain controller that is the $\mathcal{H}_\infty$ controller. Even though the SMC is superior, the $\mathcal{H}_\infty$ controller synthesized using the nominal plant is capable of controlling the CSU 4OptimX in situations were extreme accuracy in target impedance position is not necessary. This controller also produces less motor chatter. This characteristic can greatly extend the life of the CSU 4OptimX motors.

Each control law has advantages and disadvantages pertaining to design, implementation, and performance. Below is a cumulative summary comparing the advantages and disadvantages of each control law toward the application of robust impedance control.

	Sliding Mode Control	$\mathcal{H}_\infty$ Control
Advantages	Simple controller design process	Simple, fixed gain controller
	Autonomously compensates for all disturbances and non-linearities	Ability to achieve a larger range of impedances
	Ability to change impedance parameters without controller re-design	Little to no control input chatter
	Superior impedance trajectory tracking	
Disadvantages	Potential for significant control input chatter	Must specify disturbance and non-linearities during design phase
	Smaller range of achievable impedances	Challenge to determine weights for implementable controller
		Must re-design controller when changing impedances

Table IX: Advantages and Disadvantages of Controllers

These conclusions are the grounds for deciding which robust impedance controller suits a particular application.

During this thesis, observations were made about the $\mathcal{H}_\infty$ controller design process that make designing an $\mathcal{H}_\infty$ impedance controller challenging. The designation of weights for the $\mathcal{H}_\infty$ controller synthesis directly determines the performance, disturbance rejection abilities, and implementable practicality of the synthesized controller. It is a delicate balance between those three characteristics. For feedback systems, prior research dictates the proper weight shapes for successful controller synthesis and implementation. For other systems, such as systems with impedance control, the weights are not directly known and may not be as intuitive. Achieving desired performance and disturbance rejection goals may be possible, but synthesizing a practical controller with small negative closed loop poles poses a challenge to any engineer attempting to implement the $\mathcal{H}_\infty$ control law with impedance control. Future research into general weight shapes that produce practical controllers with increased performance and disturbance rejection is needed to properly understand the strengths and weaknesses of $\mathcal{H}_\infty$. In this thesis, weights are chosen based on a literature review of common weights and an iterative design process that became cumbersome. Optimization of weight shapes for robust $\mathcal{H}_\infty$ impedance control is a valuable path of research for this topic.

BIBLIOGRAPHY

[1] Paul E Colosky Jr and Tara M Ruttley. Gravity-independent constant force resistive exercise unit.

[2] Humberto De Las Casas, Hanz Richter, and Antonie Van Den Bogert. Design and hybrid impedance control of a powered rowing machine. In ASME 2017 Dynamic Systems and Control Conference, pages V001T38A002–V001T38A002. American Society of Mechanical Engineers, 2017.

[3] John C Doyle, Keith Glover, Pramod P Khargonekar, and Bruce A Francis. State-space solutions to standard h2 and h-infinity control problems. IEEE Transactions on Automatic Control, 34(8):831–847, 1989.

[4] Ray M Eid. Interim resistive exercise device, Jan 2018.

[5] Neville Hogan. Impedance control: An approach to manipulation: Part ii—implementation. Journal of Dynamic systems, Measurement, and Control, 107(1):8–16, 1985.

[6] Ming-Shaung Ju, C-CK Lin, Dong-Huang Lin, I-S Hwang, and Shu-Min Chen. A rehabilitation robot with force-position hybrid fuzzy controller: hybrid fuzzy control of rehabilitation robot. IEEE Transactions on Neural Systems and Rehabilitation Engineering, 13(3):349–358, 2005.

[7] Kazuo Kiguchi and Yoshiaki Hayashi. An emg-based control for an upper-limb power-assist exoskeleton robot. IEEE Transactions on Systems, Man, and Cybernetics, Part B (Cybernetics), 42(4):1064–1071, 2012.

[8] Kornelia Kulig, James G Andrews, and James G Hay. Human strength curves. Exercise and Sport Sciences Reviews, 12(1):417–466, 1984.

[9] Zhijun Li, Zhicong Huang, Wei He, and Chun-Yi Su. Adaptive impedance control for an upper limb robotic exoskeleton using biological signals. IEEE Transactions on Industrial Electronics, 64(2):1664–1674, 2017.

[10] Jinkun Liu and Xinhua Wang. Advanced sliding mode control for mechanical systems: design, analysis and MATLAB simulation. Springer Science & Business Media, 2012.

[11] Jean L McCrory, David R Lemmon, H Joseph Sommer, Brian Prout, Damon Smith, Deborah W Korth, Javier Lucero, Michael Greenisen, Jim Moore, Inessa Kozlovskaya, et al. Evaluation of a treadmill with vibration isolation and stabilization for use on the international space station. Journal of Applied Biomechanics, 15(3):292–302, 1999.

[12] A. Megretski. Algorithms for h-infinity optimization, March 2004.

[13] Saïd Moughamir, Alexandre Deneve, Janan Zaytoon, and Lissan Afilal. Hybrid force/impedance control for the robotized rehabilitation of the upper limbs. In Proceedings of 16th IFAC World Congress, 2005.

[14] Melissa Murray. Treadmill with vibration isolation and stabilization system, May 2018.

[15] Andre Rosenberger Tobias Weber Jonathan Scott Filippo Castrucci Nora Petersen, Patrick Jaekel. Exercise in space: the european space agency approach

to in-flight exercise countermeasures for long-duration missions on iss. Springer Nature: Extreme Physiology and Medicine, 5(9), August 2 2016.

[16] Shola Otitoju, Hanz Richter, and Antonie J Van Den Bogert. Admittance control for an electromechanical rowing machine. In 2016 IEEE International Conference on Advanced Intelligent Mechatronics, pages 142–147. IEEE, 2016.

[17] Richard J Potash, Robert L Potash, Wojciech J Krawiec, and Stephen K Burns. Asymmetric force applicator attachment for weight stack type exercise machines.

[18] Jasen L Raboin, Jason Niebuhr, Santana F Cruz, and Christopher D Lamoreaux. Advanced resistive exercise device.

[19] Hanz Richter. Advanced control of turbofan engines. Springer Science & Business Media, 2011.

[20] Hanz Richter and Dhipak Selvaraj. Impedance control with energy regeneration in advanced exercise machines. In American Control Conference (ACC), 2015, pages 5890–5895. IEEE, 2015.

[21] Sigurd Skogestad and Ian Postlethwaite. Multivariable feedback control: analysis and design, volume 2. Wiley New York, 2007.

[22] Rong Song, Kai-yu Tong, Xiaoling Hu, Le Li, et al. Assistive control system using continuous myoelectric signal in robot-aided arm training for patients after stroke. IEEE Transactions on Neural Systems and Rehabilitation Engineering, 16(4):371–379, 2008.

[23] Philip Truong. Cycle ergometer with vibration isolation and stabilization system, Dec 2018.